Compositional zoning of fluid inclusions in the Archaean Junction gold deposit, Western Australia: A process of fluid - wall-rock interaction? — Source link

Paul A. Polito, Yvonne Bone, Jonathan D. A. Clarke, Terrence P. Mernagh

Institutions: University of Adelaide, Australian National University

Topics: Fluid inclusions, Vein (geology), Wall rock and Petrography

Related papers:

- Orogenic gold deposits : A proposed classification in the context of their crustal distribution and relationship to other gold deposit types

- Distribution, character and genesis of gold deposits in metamorphic terranes

- Orogenic gold and geologic time: a global synthesis

- Fluid Chemistry of Orogenic Lode Gold Deposits and Implications for Genetic Models

- Orogenic gold: Common or evolving fluid and metal sources through time

Compositional zoning of fluid inclusions in the Archaean Junction gold deposit, Western Australia: A process of fluid - wall-rock interaction?

P. A. Polito , Y. Bone , J. D. A. Clarke & T. P. Mernagh

Compositional zoning of fluid inclusions in the Archaean Junction gold deposit, Western Australia: a process of fluid – wall-rock interaction?

P. A. POLITO,[1]* Y. BONE,[1] J. D. A. CLARKE[2] AND T. P. MERNAGH[3]

[1]*Department of Geology and Geophysics, University of Adelaide, SA 5005, Australia.*
[2]*Department of Geological Sciences, Australian National University, ACT 0200, Australia.*
[3]*Australian Geological Survey Organisation, GPO Box 378, Canberra, ACT 2601, Australia.*

The Junction gold deposit, in Western Australia, is an orogenic gold deposit hosted by a differentiated, iron-rich, tholeiitic dolerite sill. Petrographic, microthermometric and laser Raman microprobe analyses of fluid inclusions from the Junction deposit indicate that three different vein systems formed at three distinct periods of geological time, and host four fluid-inclusion populations with a wide range of compositions in the H_2O–CO_2–CH_4–NaCl ± $CaCl_2$ system. Pre-shearing, pre-gold, molybdenite-bearing quartz veins host fluid inclusions that are characterised by relatively consistent phase ratios comprising H_2O–CO_2–CH_4 ± halite. Microthermometry suggests that these veins precipitated when a highly saline, >340°C fluid mixed with a less saline ≥150°C fluid. The syn-gold mineralisation event is hosted within the Junction shear zone and is associated with extensive quartz–calcite ± albite ± chlorite ± pyrrhotite veining. Fluid-inclusion analyses indicate that gold deposition occurred during the unmixing of a 400°C, moderately saline, H_2O–CO_2 ± CH_4 fluid at pressures between 70 MPa and 440 MPa. Post-gold quartz–calcite–biotite–pyrrhotite veins occupy normal fault sets that slightly offset the Junction shear zone. Fluid inclusions in these veins are predominantly vapour rich, with CO_2>>CH_4. Homogenisation temperatures indicate that the post-gold quartz veins precipitated from a 310 ± 30°C fluid. Finally, late secondary fluid inclusions show that a <200°C, highly saline, H_2O–$CaCl_2$–NaCl-bearing fluid percolated along microfractures late in the deposit's history, but did not form any notable vein type. Raman spectroscopy supports the microthermometric data and reveals that CH_4-bearing fluid inclusions occur in syn-gold quartz grains found almost exclusively at the vein margin, whereas CO_2-bearing fluid inclusions occur in quartz grains that are found toward the centre of the veins. The zonation of CO_2:CH_4 ratios, with respect to the location of fluid inclusions within the syn-gold quartz veins, suggest that the CH_4 did not travel as part of the auriferous fluid. Fluid unmixing and post-entrapment alteration of the syn-gold fluid inclusions are known to have occurred, but cannot adequately account for the relatively ordered zonation of CO_2:CH_4 ratios. Instead, the late introduction of a CH_4-rich fluid into the Junction shear zone appears more likely. Alternatively, the process of CO_2 reduction to CH_4 is a viable and plausible explanation that fits the available data. The CH_4-bearing fluid inclusions occur almost exclusively at the margin of the syn-gold quartz veins within the zone of high-grade gold mineralisation because this is where all the criteria needed to reduce CO_2 to CH_4 were satisfied in the Junction deposit.

KEY WORDS: carbon dioxide, fluid inclusions, geochemistry, gold, Kambalda, methane, Western Australia, Yilgarn Craton.

INTRODUCTION

The Junction gold mine is an orogenic gold deposit hosted by the Fe-rich Junction Dolerite, a differentiated tholeiitic sill (Watchorn 1998). Gold mineralisation is associated with an alteration halo that represents the evolution of a fluid as it dispersed outward from a central conduit. The alteration halo is associated with an extensive quartz–calcite ± albite ± chlorite ± pyrrhotite vein assemblage. The aqueous solutions that transported gold to the site of mineralisation would have been trapped within vein material as fluid inclusions. These fluid inclusions provide an ideal opportunity to study the role of fluids in faulting, stress cycling and wall-rock interaction (Sibson *et al*. 1988; Boullier & Robert 1992; Robert *et al*. 1995).

Fluid-inclusion investigations from orogenic, lode-gold deposits in Western Australia and Canada are well documented (Robert & Kelly 1987; Clark *et al*. 1989; Ho *et al*. 1990a, b, 1992; Boullier & Robert 1992; Robert *et al*. 1995). Gold was typically transported by a low salinity H_2O–CO_2 ± CH_4-rich, alkaline to near-neutral fluid with densities of 0.7–0.8 g/cm³ (Ho *et al*. 1990a, b; Robert *et al*. 1995). Pressure estimates are usually between 70 MPa and 410 MPa, with most between 100 MPa and 300 MPa (Ho *et al*. 1990a; Boullier & Robert 1992). Homogenisation temperatures (Th) indicate that the temperature of entrapment (Tt) for this deposit type ranges from 200°C to 400°C.

*Corresponding author and present address: Department of Geological Sciences and Geological Engineering, Queen's University, Kingston, ON, K7L 3N6, Canada (polito@geol.queensu.ca).

Interpretation suggests that fluid unmixing was relatively common (Robert *et al.* 1995).

The purpose of this paper is to document the morphology and geochemistry of the fluid inclusions hosted in the various quartz veins that exist at the Junction deposit. Further, we present new data that suggests that the geochemistry of some syn-gold fluid inclusions is dependent on the interaction between the gold-bearing fluid and the Junction Dolerite. This paper emphasises Raman data that show that CH_4-bearing fluid inclusions are most common at the margin of quartz–calcite veins where wall-rock alteration is most intense, but are comparatively rare throughout the remaining vein material in which CO_2-rich fluid inclusions predominate. We investigate the possibility that the CH_4-bearing fluid inclusions are a result of fluid unmixing or post-entrapment alteration, but ultimately propose that the CH_4 is a by-product of the hot, gold-bearing H_2O–CO_2 fluid interacting with the Fe-rich host rock under reducing conditions.

GEOLOGICAL SETTING OF THE JUNCTION DEPOSIT

The Junction gold deposit is located in the southern part of the Norseman–Wiluna greenstone belt, Western Australia (Latitude 121°50′E, Longitude 31°27′S: Figure 1).

Depositional ages for the Norseman–Wiluna belt vary from 2700 Ma to 2690 Ma for the komatiitic volcanic units to 2680 Ma for the overlying felsic–metasedimentary units of the Black Flag Group (Claoué-Long *et al.* 1988; Nelson 1995). The Junction deposit is located approximately 3 km east of the Boulder–Lefroy Fault (Figure 1). Mineralisation is hypothesised to be associated with low-order branching structures off the Boulder–Lefroy Fault.

Junction is a blind deposit, covered by up to 40 m of saprolitic clay, Tertiary palaeovalley fill and reddish alluvial loam. Gold mineralisation is hosted by the Junction Dolerite, a 500 m thick, differentiated, iron-rich, tholeiitic sill. The Junction Dolerite intrudes the lower unit of the Black Flag Group making it co-equivalent to the Golden Mile Dolerite, host of the Golden Mile Deposit, Kalgoorlie (Boulter *et al.* 1987; Carey 1994). The Junction Dolerite has been regionally metamorphosed to an actinolite–hornblende–albite–chlorite–epidote–quartz assemblage indicative of upper greenschist facies metamorphic conditions (Witt 1992). The original textures in the sill have been preserved allowing it to be divided into four distinct units (not including the fine-grained upper and lower chill margins) based on petrographical as well as geochemical observations (Figures 2, 3). These units are similar in appearance, composition and texture to those described for the Golden Mile Dolerite by Phillips (1986).
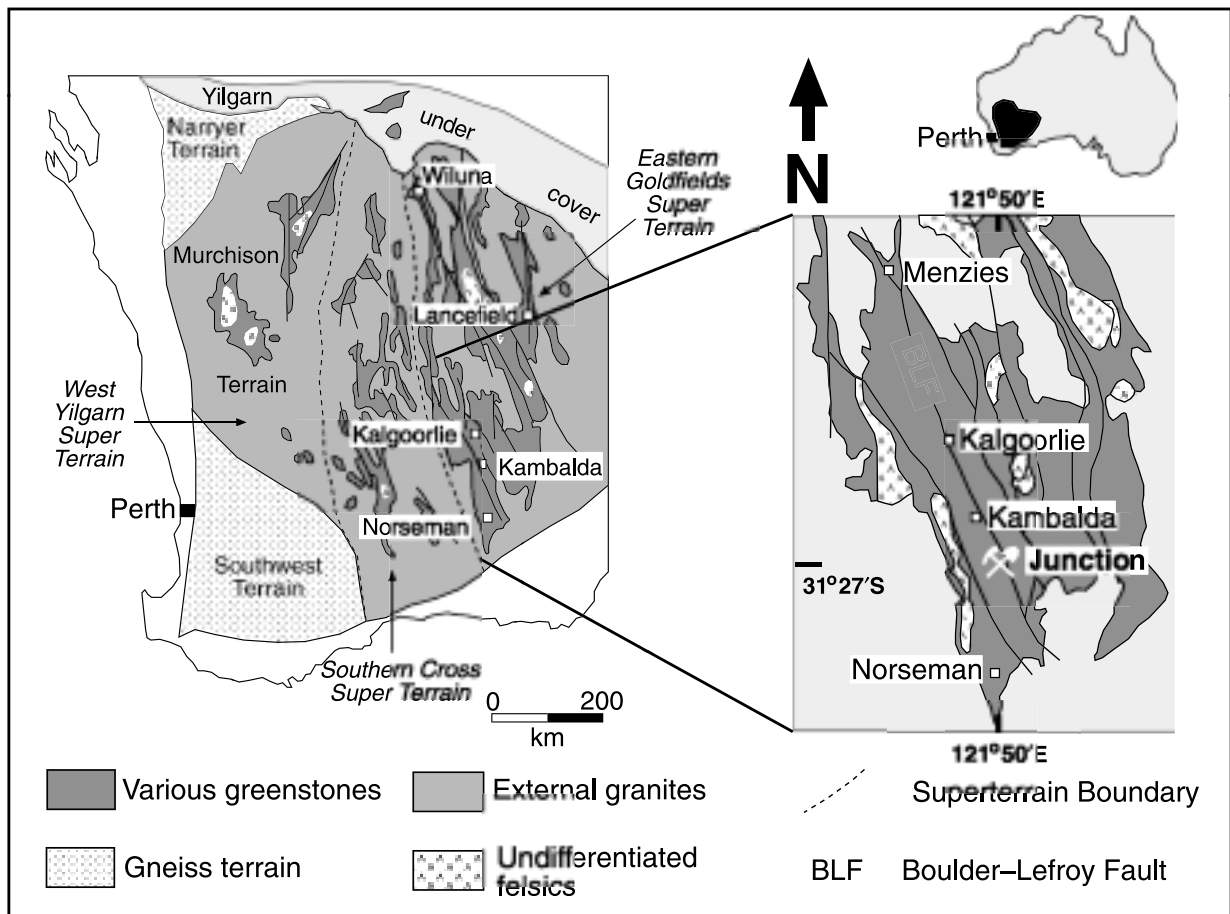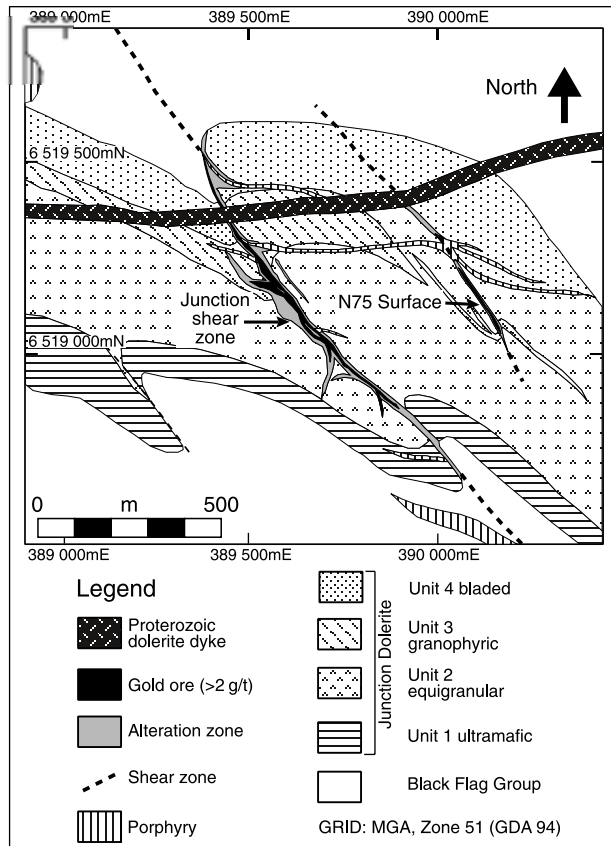

Figure 1   Regional geology of the Yilgarn Craton, Western Australia, incorporating a modified geological map of the southwestern Kalgoorlie Terrain (inset) and showing the location of the Junction deposit (compiled from figures presented in Phillips & Groves 1983 and Witt *et al.* 1998).

Figure 2 Basement geology of the Junction deposit highlighting the currently mined Junction shear zone and the related N75 surface. Map compiled from diamond drillhole and aeromagnetic data (modified from Ellery & Watts 1996).
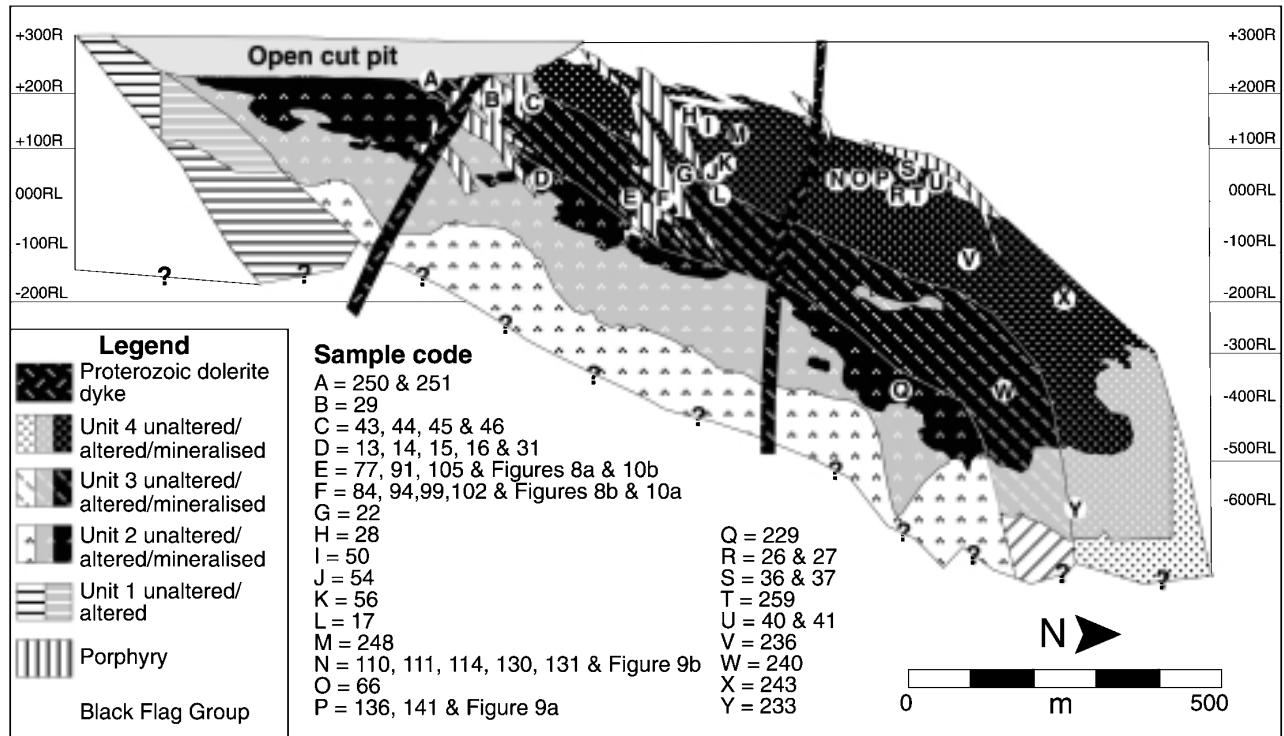
Unit 1

Unit 1 has a distinct cumulate texture and represents a weak accumulation of more mafic minerals in the basal part of the sill. Olivine and pyroxene were pseudomorphed during regional metamorphism by actinolite, lesser hornblende ± tremolite and chlorite (Carey 1994). At the same time, plagioclase was altered to a clinozoisite–epidote–calcite–albite saussurite assemblage. Oxides represent <2% of Unit 1 and consist predominantly of ilmenite, with up to 90% of the ilmenite breaking down to titanite. Secondary magnetite is rare and occurs as overgrowths on amphiboles.

Unit 2

Unit 2 has an equigranular, porphyritic texture marked by dark-green, equant hornblende and paler elongate actinolite that are pseudomorphs after orthopyroxene and clinopyroxene, respectively. The hornblende and actinolite make up 45–50% of Unit 2, with actinolite becoming slightly more abundant toward the transition to Unit 3. Electron microprobe data show that the orthopyroxene was superseded by clinopyroxene towards its transition to Unit 3 prior to regional metamorphism (Carey 1994).

Figure 3 Longitudinal cross-section through the Junction shear zone showing the four units of the Junction Dolerite in relation to gold mineralisation. In this diagram, mineralised refers to drillhole intersections that graded >2 ppm Au (equivalent to the biotite–calcite zone), whereas altered refers to both the chlorite zone and albite zones in which gold grades are <2 ppm. Samples used for fluid-inclusion analysis and/or referred to in the text are labelled as indicated. RL, relative sea-level. Question marks at base of Junction Dolerite and Black Flag Group represent drillhole limits and indicate that both units extend to an unknown depth. Diagram modified from maps constructed by WMC geologists. All rock samples are held at the Department of Geology and Geophysics, University of Adelaide, Adelaide.

Albite makes up to 50% of Unit 2. It is present as either distinct laths or as an interstitial phase. There is an increase in the size of albite laths as the sill grades into Unit 3. The overall textures of Unit 2 suggest simultaneous plagioclase–pyroxene crystallisation.

A gradual transition from Unit 1 to Unit 2 is marked, among other features, by a change in the oxide species from ilmenite to titanomagnetite. The titanomagnetite is largely altered to titanite and rutile. With increasing proximity to Unit 3, the oxide species rapidly changes back to ilmenite, which has a characteristic skeletal form.

Unit 3

Unit 3 is a highly differentiated granophyre. It exhibits a diffuse textural change across the boundaries between Units 2 and 4, a feature attributed to recrystallisation of this unit by late-stage deuteric fluids (Carey 1994). Granophyric intergrowth between albite and quartz gives Unit 3 a distinct texture. Coarse-grained albite laths (up to 7 mm) make up 55% of Unit 3, with the rest of the unit generally composed of quartz, hornblende and rarer actinolite. Saussurite alteration characterised by a relatively coarse euhedral epidote phase formed from the breakdown of igneous Ca-rich plagioclase.

Unit 3 represents the last magma to crystallise in the sill and marks the peak of the sill's differentiation trend. It has the highest iron and incompatible element content. Ilmenite and magnetite coexist, either as homogeneous grains or as an exsolution of one within the other. The two oxides make up approximately 12% of Unit 3 and probably formed during the exsolving of titanium from titanomagnetite during oxidation associated with cooling (Vaughan & Craig 1997).

Unit 4

Unit 4 has a typically bladed texture until it passes sharply into the fine-grained upper chilled margin of the sill. Orthopyroxene and clinopyroxene were pseudomorphed during regional metamorphism by actinolite and hornblende, respectively (Carey 1994) and comprise 45–50% of Unit 4. Saussurite replacement of fine-grained albite, quartz and actinolite make up 45–50% of the unit. Textures indicate that plagioclase and pyroxene were crystallising simultaneously (Carey 1994).

Geochemically, Unit 4 is moderately enriched in the incompatible elements, iron and titanium, when compared to Unit 1 or the base of Unit 2. Ilmenite is the dominant oxide present in Unit 4.

Porphyry dykes

The Junction Dolerite is intruded by a number of felsic, porphyry dykes (Figure 3). These dykes have been classified as either porphyritic micro-quartz monzodiorite or porphyritic hornblende-bearing micro-quartz monzodiorite (Murphy 1995). The porphyry dykes have insignificant chilled margins where they contact the Junction Dolerite, suggesting intrusion at the time of peak metamorphism and before the development of the Junction shear zone (Murphy 1995).

Proterozoic dolerite dykes

Two east–west-striking Proterozoic dolerite dykes cross-cut the Junction deposit (Figure 3). These dykes are 20–30 m wide, dip steeply to the south, and dextrally displace the ore lodes by up to 20 m. They consist predominantly of calc-plagioclase, augite, hornblende, biotite, quartz and chlorite, and exhibit chilled margins at the contact with the Junction Dolerite.

MINERALISATION AND HYDROTHERMAL ALTERATION

The main gold lode at Junction is structurally controlled in the northwest-trending Junction shear zone. Smaller, but significantly mineralised, shear zones, such as the N75 surface, mostly trend subparallel to the Junction shear zone (Figure 2). The Junction shear zone cross-cuts all units of the Junction Dolerite and dips to the northeast at approximately 40° (Roberts & Elias 1990). It is interpreted as a reverse-oblique shear zone with the east block up and north, as determined by slickenside fibres on shear surfaces. Economic gold grades (>2 g/t) are present in Units 2, 3 and 4 of the Junction Dolerite, but are mostly focused in the iron oxide enriched Units 3 and 4 (Figure 3).

Gold mineralisation is associated with a wall-rock alteration halo that has overprinted the regional metamorphic assemblage in the Junction Dolerite. Wall-rock alteration can be divided into three discrete zones: the outer albite zone, the intermediate chlorite zone and the inner biotite–calcite zone (Figure 4). These discrete alteration zones indicate that gold deposition was principally invoked by interaction between the ore fluid and the Fe-rich host rocks. However, as we will show, fluid inclusions suggest that phase separation and fluid unmixing also occurred.

Albite zone

The outer albite zone comprises amphibole–albite–chlorite–ilmenite–titanomagnetite–ankerite–calcite–quartz–pyrrhotite ± pyrite–biotite. The albite zone has mostly retained the 'igneous' texture of the Junction Dolerite, despite widespread alteration, although it can be weakly foliated in places. The albite zone has a gradational outer boundary extending into the unaltered Junction Dolerite, and has a sharp contact with the texturally destructive chlorite zone. The width of the albite zone ranges from 0.5 m to 3.0 m and gold grades are generally <0.1 ppm. Alteration is dominated by partial to complete replacement of pseudomorphic amphibole with randomly orientated chlorite and acicular amphibole. Large albite laths containing solid inclusions of chlorite, biotite and amphibole are observed replacing fine-grained saussurite. Minor, fine-grained biotite is observed rimming saussurite where it is in contact with altered amphibole, titanomagnetite and ilmenite grains. Minor calcite ± ankerite is observed as veinlets, and makes up to 10% of the wall-rock alteration assemblage near quartz veins. Quartz veins are not common and are generally the extensional vein type discussed below.

Chlorite zone

The intermediate chlorite zone ranges from 0.5 m to 2 m wide and gold values are <1.0 ppm. The boundary between the chlorite zone and the biotite–calcite zone is gradational. The intermediate chlorite zone is distinguished from the inner biotite–calcite zone and the outer albite zone by the abundance of fine-grained chlorite intergrown with fine-grained biotite, quartz, albite, calcite, magnetite, ankerite and pyrrhotite. Chlorite and biotite comprise approximately equal proportions in this zone, collectively making up to 45% of the alteration assemblage. Both chlorite and biotite replace amphibole, and rarely titanomagnetite and ilmenite. Foliation is weakly to moderately developed, but is clearly defined by the orientation of the chlorite and biotite. Extensional quartz veins are common, but not overly prevalent. Albite and calcite is often present at the margins of these veins. Calcite and lesser ankerite are common in the quartz veins and as matrix minerals. Calcite occupies up to 20% of the alteration assemblage. Calcite is regularly found within the skeletal structure of ilmenite and titanomagnetite, where it coexists with rutile. Trace amounts of magnesite are present in altered areas in Unit 1 of the Junction Dolerite. Titanomagnetite, and to a lesser extent, biotite are replaced by pyrrhotite ± pyrite toward the inner biotite–calcite zone boundary.

Biotite–calcite zone

Gold is principally located within the inner biotite–calcite zone. This zone ranges from 3 m to 10 m in width and gold grades are generally >2 ppm. The dominant minerals in the biotite–calcite zone, in order of abundance, are quartz–calcite–albite–biotite–chlorite–pyrrhotite. Mineralisation associated with a biotite–calcite–quartz–albite–pyrrhotite ± pyrite alteration assemblage in mafic host rocks indicates formation temperatures of 400°C (Witt *et al*. 1997).

The majority of quartz is present as vein material, but subordinate amounts are present throughout the alteration matrix. Albite is common throughout the biotite–calcite zone and is particularly notable in the matrix around the edges of and within the quartz veins. Biotite is the dominant mica in the alteration matrix where it defines a moderate to pervasive foliation that occasionally grades into mylonite. In Unit 4 of the Junction Dolerite, biotite and chlorite coexist. However, chlorite is significantly less abundant from the equivalent alteration assemblage in Unit 3 where there is an increase in the biotite and calcite content.

Carbonate alteration is an important feature in the Junction shear zone and four carbonate phases are present in varying proportions in different units of the Junction Dolerite. Calcite is the dominant carbonate phase in the biotite–calcite zone and is present throughout all units of the Junction Dolerite. It can comprise up to 40% of the matrix alteration assemblage, particularly near quartz veins. It is typically ubiquitous with sulfide mineralisation and is often observed in quartz veins. Formation temperatures, calculated by oxygen isotope geothermometry formed on coexisting hydrothermal quartz and calcite vein samples using the equation $1000\ln\alpha = 0.6(10^6/T^2)$ (where T is in degrees Kelvin) based on experimental methods published by O'Neil *et al*. (1969) and Clayton *et al*. (1972), cluster between 381°C and 434°C (range 289–465°C; Table 1) (Polito 1999). This is in agreement with the mineral equilibria temperature estimate proposed by Witt *et al*. (1997).
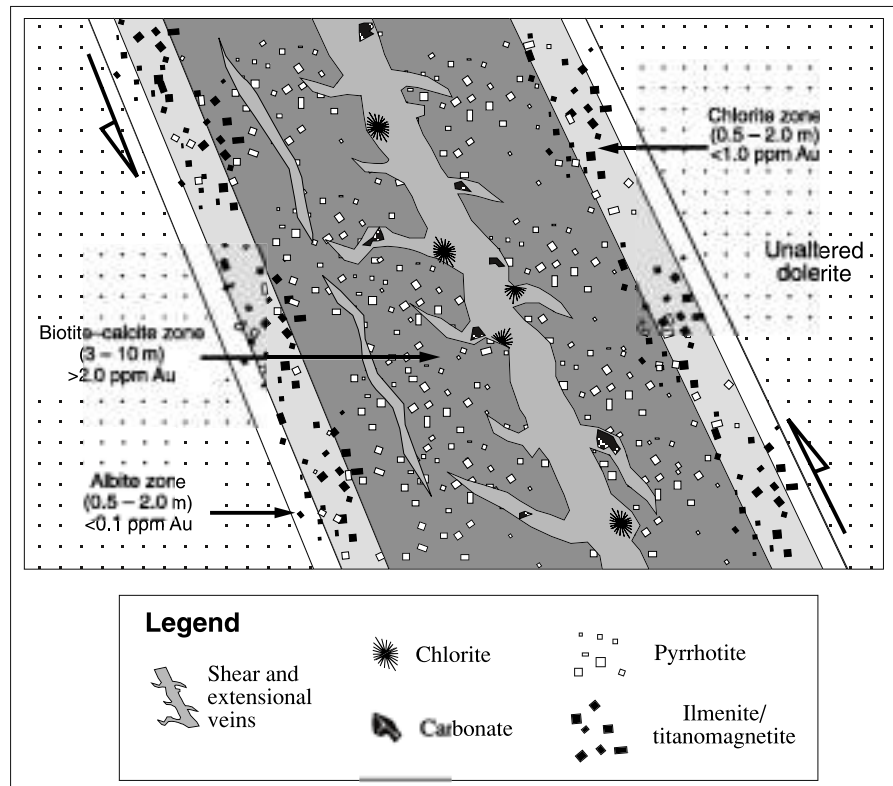
Figure 4 Idealised sketch through a mineralised section of the Junction shear zone (Units 2, 3 or 4) showing the relationship between the biotite–calcite zone, the chlorite zone and the albite zone.

Electron microprobe analysis and cathodoluminescence microscopy show that calcite varies in composition from Fe-rich to Fe-poor within individual veins and crystals (Figure 5a). The Fe-poor calcite is typically later than the

Number and position of points analysed by electron microprobe

— % Fe   — % Mg   — % Mn
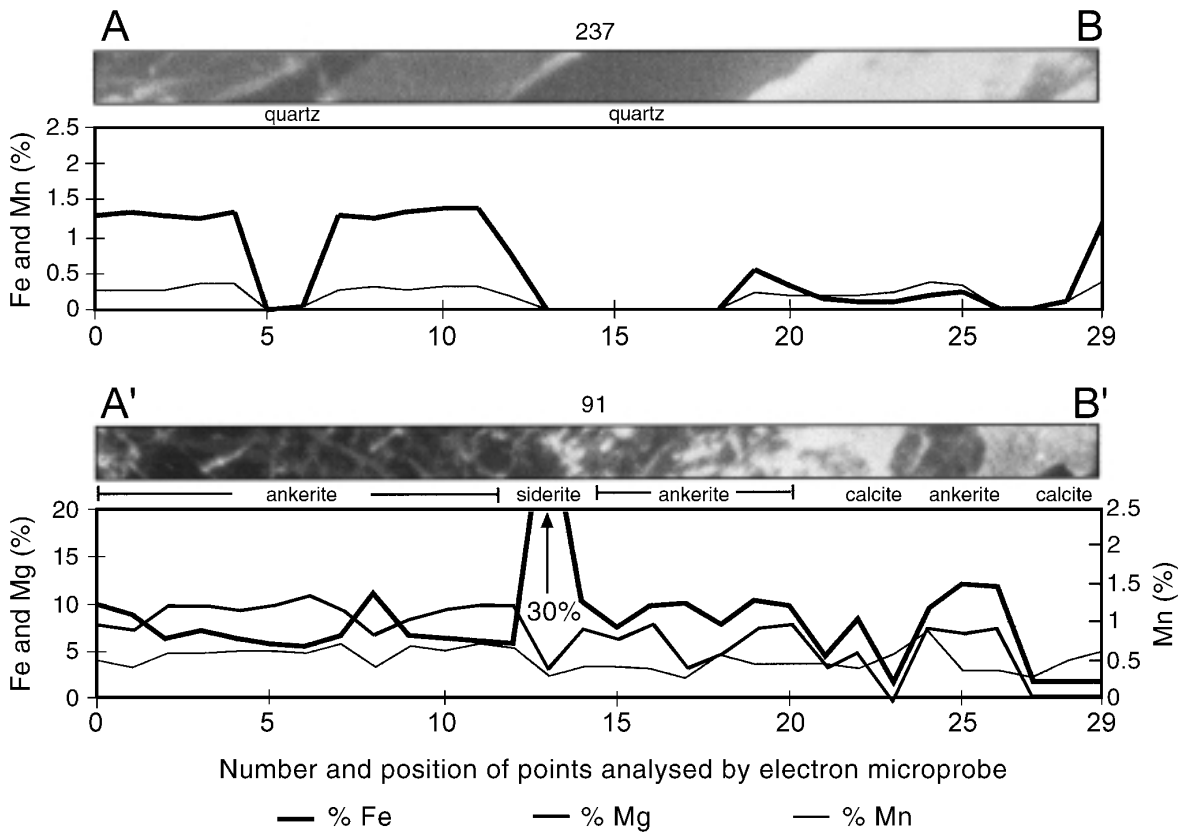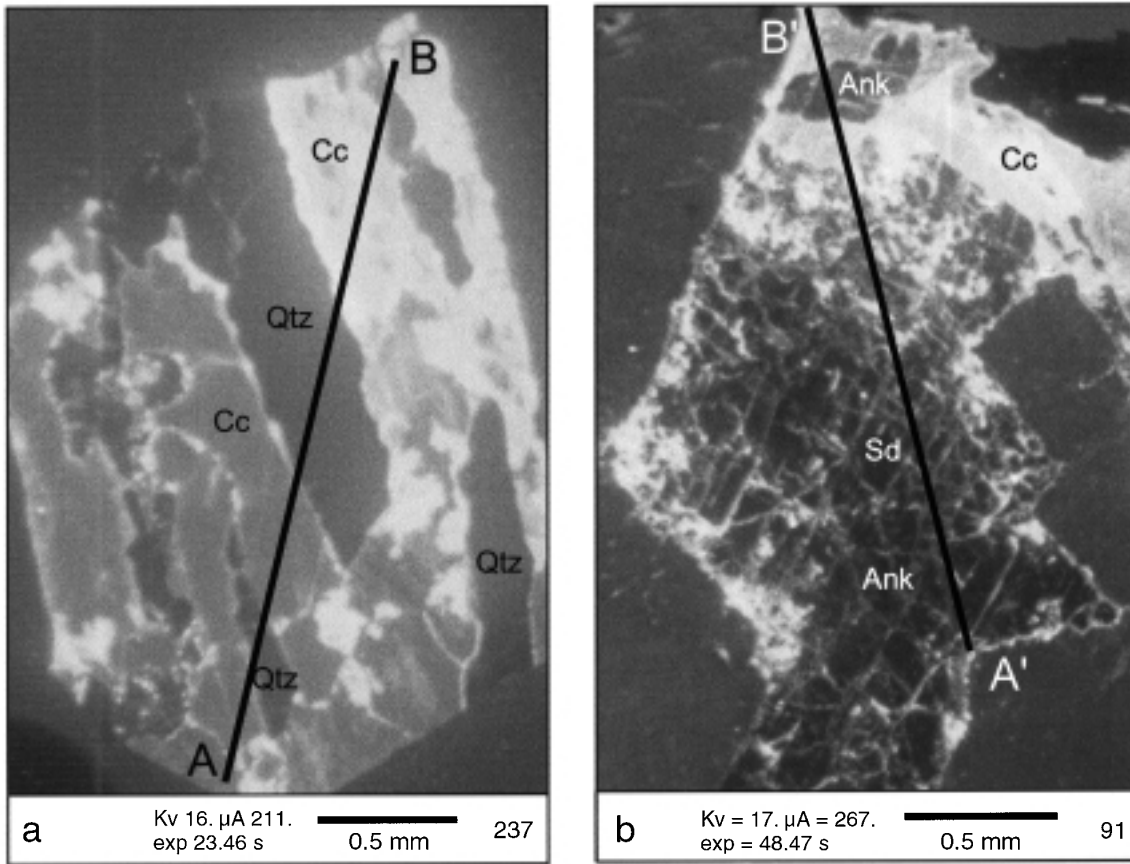
Fe-rich calcite and is most common in areas where pyrrhotite is particularly abundant. This suggests that the chemical composition of the calcite is a function of the competition for Fe by sulfur to form sulfides in the inner biotite–calcite zone.

Ankerite is present in the biotite–calcite zone, but subordinate to calcite in Units 3 and 4 of the Junction Dolerite. Ankerite is known to coexist with rare siderite (Figure 5b). Cathodoluminescence microscopy shows that calcite replaces the ankerite and siderite along their margins and cleavage planes (Figure 5b). Magnesite is present in minor amounts in the more mafic areas of the Junction Dolerite, principally at the base of Unit 2 and at the top of Unit 4.

Scanning electron microscopy analyses and reflected-light petrography show that titanomagnetite, and to a lesser extent ilmenite, are still present, but relatively rare in the biotite–calcite zone (Figure 6). Pyrrhotite ± chalcopyrite ± pyrite, calcite and rutile replace titanomagnetite, ilmenite and occasionally biotite. Gold is predominantly associated with pyrrhotite and pyrite mineralisation, but it also occurs as free grains in some quartz veins. Pyrite dominates over pyrrhotite in the upper levels of the deposit and its presence corresponds to mineralisation that occurs in the relatively Fe-poor Unit 2 of the Junction Dolerite. Reflected-light petrography shows that the dominance of pyrite over pyrrhotite in Unit 2 is not due to supergene replacement of pyrrhotite by pyrite. In Units 3 and 4, pyrrhotite dominates over minor chalcopyrite and negligible pyrite. Chalcopyrite is relatively common (<5% of the total sulfide species) in most parts of Units 3 and 4, often coexisting as blebs around pyrrhotite (Figure 6).

VEIN STYLES AND RELATED FLUID-INCLUSION MORPHOLOGY

Three main generations of quartz veins represent different periods of tectonic activity: (i) pre-shearing, pre-gold, molybdenite-bearing quartz veins; (ii) syn-shearing,

Table 1 Oxygen isotope results and geothermometric calculations for coexisting quartz and calcite.

Sample No.	δ¹⁸O calcite	δ¹⁸O quartz	Geothermometry temperature (°C)
Biotite–calcite zone			
84	11.2	12.8	339
94	10.4	11.8	381
99	10.4	11.6	434
105	11.8	12.9	465
110	10.7	11.9	434
111	10.7	12.4	321
114	10.6	12.4	304
141	10.7	12.0	406
236	10.1	11.3	434
251	10.2	12.1	289
Post-gold quartz vein			
77	9.8	11.3	359
130	9.3	11.1	304
136	9.7	11.6	289

Calculated using the equation $1000\ln\alpha = 0.6(10^6/T^2)$ based on experimental methods published by O'Neil *et al.* (1969) and Clayton *et al.* (1972).

Figure 5 Cathodoluminescence photomicrographs and electron microprobe traverses (lines A–B and A′–B′). (a) Sample 237 showing the effect that Fe variation relative to Mn has on luminescence within calcite in an extensional quartz–calcite vein with elongate mineral fibres. Note the occurrence of the bright luminescent calcite with lower Fe concentration rimming and replacing the dull luminescent Fe-calcite. (b) In sample 91, the high Fe content of the ankerite and siderite quenches most of the luminescence, whereas the calcite with its lower Fe content is much brighter and is clearly replacing the ankerite and siderite around their margin and cleavage planes. Qtz, quartz; Cc, calcite; An, ankerite; Sd, siderite. Thin-sections are held by P. A. Polito at Queen's University, Kingston, ON, Canada.
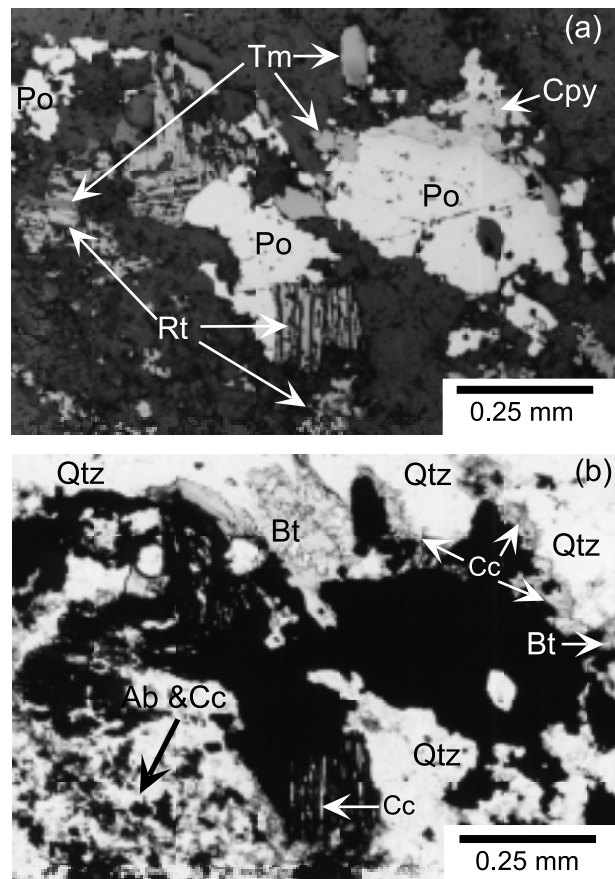

Figure 6 (a) Transmitted light and (b) reflected light photomicrographs of sample 13 showing the replacement of titanomagnetite (Tm; with remnant exsolution texture, upper left and lower centre) by rutile (Rt), pyrrhotite (Po), chalcopyrite (Cpy) and calcite (Cc). Although not clearly evident in these photomicrographs, cathodoluminescent photomicrographs clearly show that calcite and, less commonly, ankerite rim the pyrrhotite and chalcopyrite and often infill and preserve the former exsolution sites between the rutile (e.g. the white areas in Figure 5a between the cubic rutile crystal, lower centre). The area indicated by the arrow labelled Ab & Cc is mixed, fine-grained calcite, albite and rutile. Albite, biotite (Bt) and quartz (Qtz) are coexisting accessory minerals in this figure. Thin-sections are held by P. A. Polito at Queen's University, Kingston, ON, Canada.

syn-gold, quartz–calcite–albite ± biotite ± pyrrhotite ± ankerite veins; and (iii) post-shearing, post-gold, quartz–calcite–pyrrhotite–biotite veins.

Pre-shearing, molybdenite-bearing quartz veins

Molybdenite-bearing quartz veins (Mo-type quartz veins) are regularly encountered in drillholes and mine drives in the upper parts of the Junction deposit, but become less prevalent with depth from 200 m below the surface. The veins are typically laminated, and contain ribbons, clusters, plates or disseminations of molybdenite. Mo-type quartz veins are cross-cut by syn-shearing foliation and are occasionally stretched into boudins.

Quartz grains in the Mo-type quartz veins are often recrystallised, have sutured boundaries with 120° triple points and undulose extinction. Relatively undeformed quartz grains are occasionally found in embayments, protected by layers of molybdenite and chlorite in which the effects of recrystallisation were apparently minimised. These grains contain well-preserved fluid-inclusion populations that are distinct from those found in syn- or post-gold quartz veins.

FLUID INCLUSIONS IN THE MOLYBDENITE-BEARING QUARTZ VEINS

Most fluid inclusions in the Mo-type quartz veins are decrepitated or are too small to analyse by microthermometry. Useable primary fluid inclusions in the Mo-type quartz veins are only preserved in the undeformed quartz surrounded by ductile molybdenite–chlorite mineralisation. A similar form of preservation is reported by Ho *et al.* (1990b) and Spry *et al.* (1996).

Preserved fluid inclusions in Mo-type quartz veins are tabular to slightly rounded in shape. They are typically <10 μm in size. These fluid inclusions are predominantly H_2O-rich. They occasionally contain a carbonic vapour phase that generally occupies <50 vol%, and may or may not contain a halite daughter mineral (Figure 7a). Rarely, halite and another trapped mineral identified only as belonging to the carbonate group are observed in the same fluid inclusion.

Syn-gold quartz veins

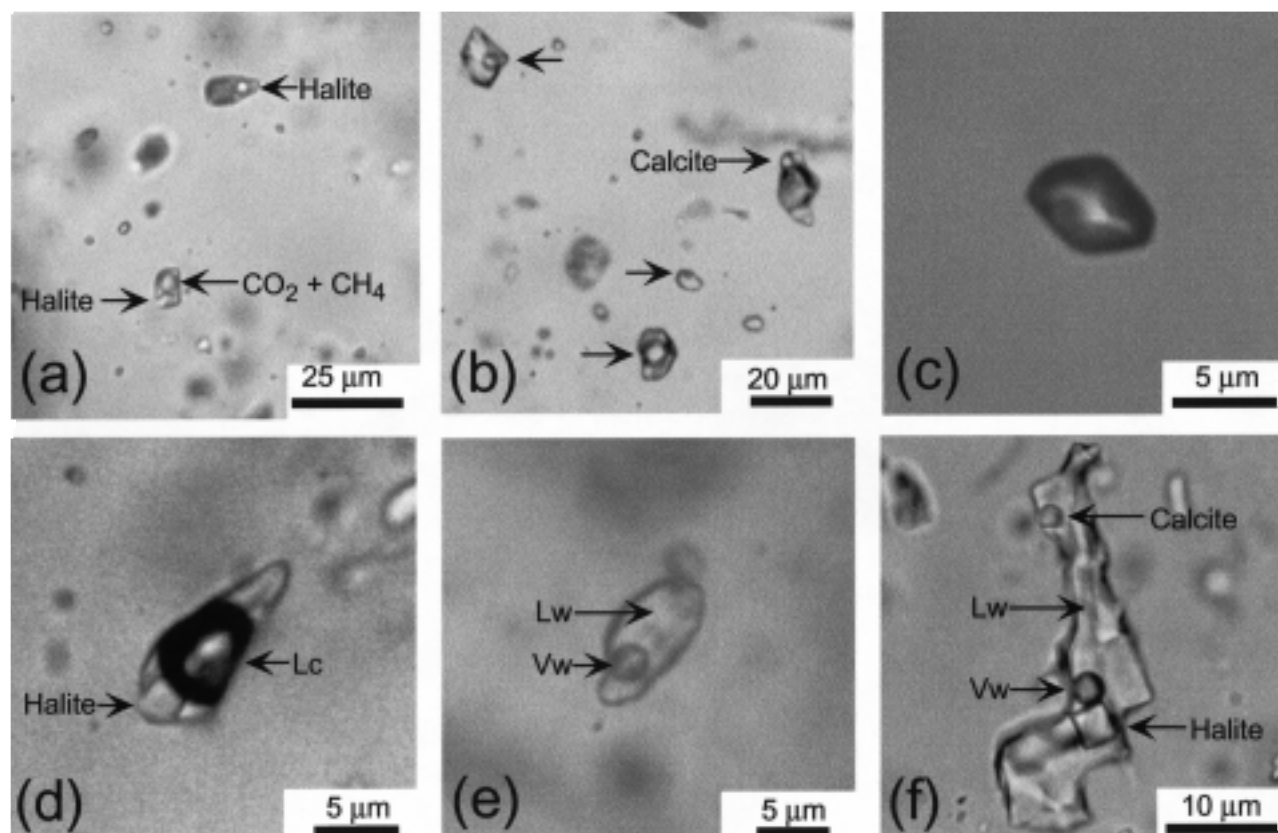Three morphological types of gold-bearing quartz veins spatially associated with the alteration assemblage at

Figure 7 Fluid-inclusion types in the Junction deposit. (a) Fluid inclusions from a Mo-type quartz vein (sample 66) containing H_2O–CO_2–CH_4 and a halite daughter minerals. (b) A 3-D cluster of fluid inclusions found in a syn-gold shear vein (sample 84) displaying a spectrum of the types of fluid inclusions created by fluid unmixing/phase separation. The three largest fluid inclusions in focus have different phase ratios varying from 15 to 70 vol% vapour. The largest fluid inclusion also contains a rare calcite daughter mineral. (c) A typical Type-A fluid inclusion in a syn-gold quartz–calcite extensional vein (sample 17) with no visible liquid phase. (d) A Type-B fluid inclusion in a syn-gold quartz–calcite shear vein (sample 250) containing >50 vol% vapour and a rare, but prominent, halite daughter mineral (Lc, liquid CO_2). (e) A Type-C fluid inclusion in a syn-gold quartz–calcite shear vein (sample 41) containing <20 vol% vapour phase (Lw, liquid water; Vw, vapour water). (f) An unusually large, but typically irregular, late secondary fluid inclusion in a syn-gold quartz–calcite shear vein (sample 41) containing two daughter minerals, calcite and halite (Lw, liquid water; Vw, vapour water). Thin-sections are held by P. A. Polito at Queen's University, Kingston, ON, Canada.

Junction were identified. All of these veins contain a diverse range of fluid-inclusion types that have compositions from CO_2-rich, to H_2O-rich. The vein types are: (i) central and oblique shear veins; (ii) horizontal to sigmoidal extensional veins; and (iii) 'jigsaw-style' breccia veins.

The three vein types are preferentially located within the Junction shear zone, but some horizontal to sigmoidal extensional veins are observed extending into the undeformed Junction Dolerite. The three vein types are mainly composed of quartz and contain subordinate albite, calcite and chlorite, minor pyrrhotite, scheelite and biotite, trace ankerite, free gold, chalcopyrite and very rarely pyrite. They are termed quartz–calcite veins. All of the vein types cross-cut one another, a feature typical of this deposit style (Robert *et al*. 1994, 1995). However, almost all veins display a similar paragenesis. Within the veins, albite, calcite and chlorite precipitate early and are typically found at the margins of the quartz veins (Figure 8a). Occasionally, quartz, biotite and pyrrhotite, trace to negligible ankerite and rare scheelite coexist with the albite, calcite and chlorite. These minerals are generally coeval with one another and are often intergrown along cleavage planes or crystal boundaries. This assemblage can vary in thickness from <1 mm to 2 cm along the vein margin. Quartz is the dominant vein mineral and many veins are monomineralic quartz in the centre of the vein (Figure 8a). Chlorite rosettes, euhedral pyrrhotite and occasionally euhedral calcite occur up to a few centimetres away from the vein – wall-rock margin, where they are encompassed by quartz. Gold is observed almost exclusively within or adjacent to the pyrrhotite. Occasionally, it clearly post-dates pyrrhotite and occurs along healed microfractures within the pyrrhotite. Free gold is present in some quartz veins.
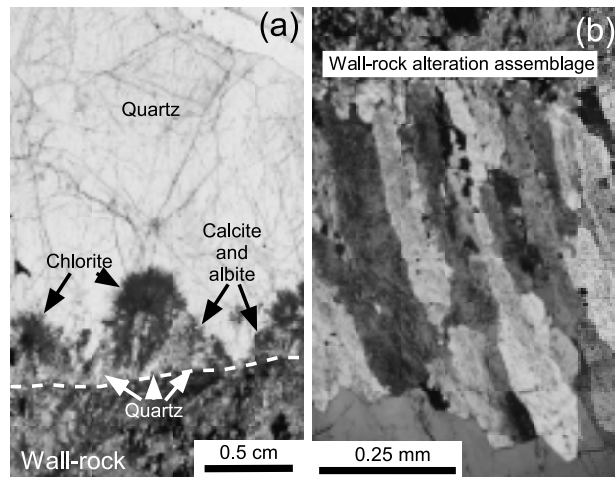
Shear veins are the most common veins at Junction. They vary in thickness from <1 cm ribbons to 3 m-wide laminated structures (Figure 9a). Quartz laminations are common in the large shear veins, but crack–seal structures were not regularly observed.

Extensional veins vary in thickness from millimetres to <1 m. At the macroscale, and with few exceptions, sigmoidal and horizontal extensional veins at Junction terminate within or at the edge of the hangingwall and footwall shears. Sigmoidal extensional veins at Junction commonly fringe shear veins and are often restricted in lateral extent, and to one side of the shear vein (Figure 9a). Horizontal extensional veins are not laterally restricted and exhibit various degrees of rotation, occasionally forming sigmoidal *en échelon* vein sets.

The most common textures and structures observed in the extensional veins at Junction are growth layering, open-space filling and elongate mineral fibres. Growth layering in extensional veins is seen at both the mesoscale and the microscale. In extensional veins, growth layers, which form during vein growth, incorporate the wall-rock and vein

Figure 8 (a) A transmitted light photoscan of a polished thin-section from a syn-gold, extensional quartz–calcite vein (sample 91) showing radiating chlorite intergrowing with calcite and albite at the vein margin. The chlorite texture is indicative of open-space filling (Robert *et al*. 1995). The dashed line defines the contact between the vein and the wall rock. Note the monomineralic quartz with abundant fluid-inclusion trails that occurs <1 cm from the wall-rock contact. (b) A transmitted light photomicrograph showing quartz mineral fibres that have formed perpendicular to the edge of the vein wall in a syn-gold quartz–calcite extensional vein (sample 102). Thin-sections are held by P. A. Polito at Queen's University, Kingston, ON, Canada.

Figure 9 (a) An example of a syn-gold quartz–calcite, reverse fault-fill shear vein (trending bottom left to upper right of photo) with related extensional veins forming in the footwall (horizontal to subhorizontal veins occurring below shear vein). Note the two post-gold quartz veins cross-cutting the shear and extensional veins (middle top to bottom right of photo). Photograph taken at location P, Figure 3. (b) Growth layering in an extensional vein from location N, Figure 3. Note the incorporation of chlorite–calcite slivers from the wall rock into the quartz vein during subsequent extension, indicating that the quartz at the edge of the vein is younger than the quartz at the centre of the vein. Coin is 29 mm in diameter.

assemblage albite–chlorite–calcite ± biotite into the vein as slivers (Figure 9b). Open-space filling textures are characterised by well-developed euhedral and radiating aggregates of chlorite, calcite, biotite and occasionally pyrrhotite crystals (Figure 8a). Mineral fibres are common in many extensional veins at Junction. They are generally perpendicular or at a high angle to the vein wall (Figure 8b).

Two styles of breccia veins occur at Junction. The most common form consists of angular wall-rock fragments set in a matrix of hydrothermal quartz (Figure 10a). These 'jigsaw-style' or 'carrot' breccia veins vary in size, but are generally <2 m wide. They are typically irregular in shape. The less common style of breccia comprises angular and rounded clasts of highly altered wall rock and vein material set in a hydrothermal matrix of albite, calcite and quartz (Figure 10b).

FLUID INCLUSIONS IN THE SYN-GOLD QUARTZ VEINS

Fluid inclusions are common in all of the syn-gold quartz veins. They can be rectangular, tabular, rounded, irregular or negative crystal shape. Their size ranges from <1 μm to ~30 μm. Compositionally, fluid inclusions in syn-gold quartz veins are diverse and range from vapour-rich to aqueous-rich, with the majority having intermediate compositions somewhere between these two end members (Figure 7b).

The fluid inclusions in syn-gold quartz veins predominantly occur along healed microfractures in the quartz. These fluid-inclusion trails are secondary relative to the host crystal, but the development of these fluid-inclusion trails is considered to be an integral part of the cyclic development of veining in a shear zone (Robert & Kelly 1987; Boullier & Robert 1992; Robert *et al.* 1995). These 'early secondary' fluid inclusions are treated with the same significance as primary fluid inclusions and are distinguished from the late secondary fluid inclusions described below. In most cases, individual trails contain fluid inclu-

sions with constant liquid to vapour ratios. The trails may cross many quartz grains or terminate at the edge of a single quartz grain (Figure 11). Less commonly, fluid inclusions occur as irregular, 3-D clusters in some quartz grains.

Vapour-rich, CO_2-dominated fluid inclusions (>80% vapour) hosted in the syn-gold quartz veins are termed Type-A fluid inclusions. Type-A fluid inclusions are common in both shear veins and extensional veins. They occur in 3-D arrays as well as being confined to fluid-inclusion trails. Type-A fluid inclusions are typically tabular, but negative crystal shapes are common (Figure 7c). Type-A fluid inclusions found along healed microfractures are typically small (<2 μm), although where they occur in 3-D clusters, they can be up to 10 μm in size.

Fluid inclusions that are hosted in the syn-gold quartz veins and have vapour to water ratios that fall between 20% and 80%, are termed Type-B fluid inclusions. They are H_2O–CO_2 fluid inclusions that are intermediate between the vapour-rich Type-A fluid inclusions and the aqueous-rich Type-C fluid inclusions described below. Type-B fluid inclusions are the most common fluid-inclusion type in the syn-gold quartz veins. Fluid inclusions with water to vapour ratios between 40% and 60% are most common. CO_2 is common in both a liquid and vapour state. Type-B fluid inclusions are frequently found as 3-D arrays, but more commonly occur along healed microfractures. They vary in size from <1 μm to 20 μm. Daughter minerals such as halite and/or trapped minerals such as nahcolite, calcite and siderite occur rarely in some Type-B fluid inclusions (Table 2; Figure 7d).

Aqueous-rich, H_2O-dominated fluid inclusions (<20% vapour) hosted in the syn-gold quartz veins are termed Type-C fluid inclusions. They are common along healed microfractures, but also occur in 3-D arrays, particularly within the shear veins. Type-C fluid inclusions are mostly
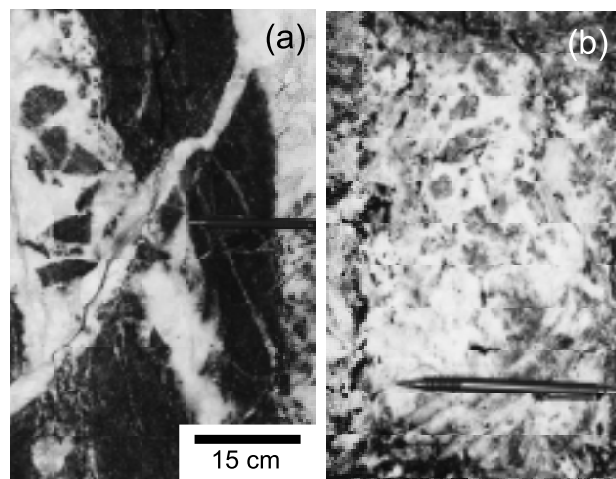

Figure 10   (a) Syn-gold, jigsaw-puzzle breccia. The most common form of breccia observed at Junction. Photograph taken at location F, Figure 3. (b) Alternatively, angular and rounded clasts of highly altered wall rock and vein material set in a hydrothermal matrix dominated by quartz and albite. A less common form of breccia. Photograph taken at location E, Figure 3.
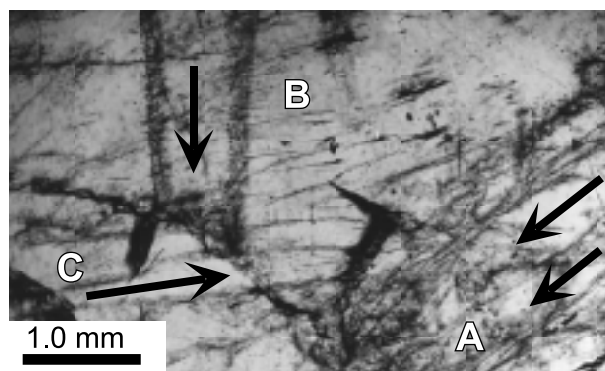
Figure 11   Transmitted light photomicrograph of fluid-inclusion trails in a syn-gold quartz–calcite shear vein. The fluid-inclusion trails in this sample reveal three increments of vein growth and deformation. The oldest of the three grains (A) contains abundant fluid-inclusion trails that appear randomly orientated. The arrows in the grain highlight the fluid-inclusion trails that terminate at the edge of this quartz grain. The next oldest quartz grain (B) contains fewer fluid-inclusion trails and only two fluid-inclusion trail orientations can be seen. The arrows in this grain highlight the fluid-inclusion trails that terminate at the edge of this quartz grain. Fluid-inclusion trails in the youngest quartz grain (C) have only one 'east–west' orientation (indicated by arrow). However, these fluid-inclusion trails cut across the other two quartz grains.

tabular to rounded (Figure 7e). Their size ranges from <1 μm to 30 μm. CO_2 is not readily identified at room temperature in most of these fluid inclusions, but was confirmed as a component in many Type-C fluid inclusions by low-temperature microthermometric reactions and Raman spectroscopy. Halite daughter minerals are present in some of these fluid inclusions.

Post-gold quartz veins

Post-gold quartz veins cut through all rock units and vein arrays in the Junction deposit (Figure 9a). They occur in southeast-dipping fault planes that show a normal sense of movement. Displacement is typically <5 cm. These veins formed after activity on the Junction shear zone ceased.
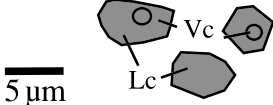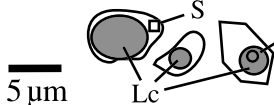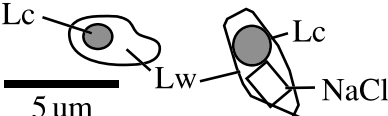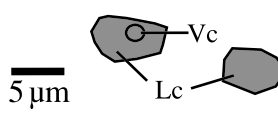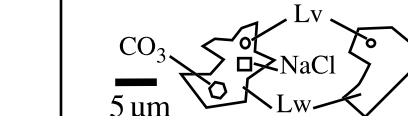
Fluid inclusion type	Type A CO_2 rich	Type B H_2O-CO_2	Type C H_2O-NaCl
Shear vein	none analysed	Vol.% CO_2 = 20 – 80 Tm_{CO_2} = -62.1 to -56.6°C Th_{CO_2} = 1.2 – 30.1°C Tfm = -61.5 to -18.6°C Tm_{ICE} = -13.2 to -0.8°C Tm_{CLATH} = 2.8 – 9.4°C Th = 223.0 – 388.6°C Td = 188.9 – 311.2°C Salinity = 1.4 – 17.1 wt% NaCl eq. CO_2 density = 0.6 – 0.92 g/cm^3	Vol.% CO_2 = 10 – 20 Tm_{CO_2} = -58.7 to -56.1°C Th_{CO_2} = 9.8 – 26.1°C Tfm = -54.4 to -16.8°C Tm_{ICE} = -9.6 to -0.8°C Tm_{CLATH} = 6.0 – 6.3°C Th = 204.8 – 373.8°C Td = none Salinity = 1.4 – 13.5 wt% NaCl eq. CO_2 density = 0.7 – 0.83 g/cm^3
Extensional vein	Vol.% CO_2 = 90$^+$ Tm_{CO_2} = -57.6 to -56.7°C Th_{CO_2} = -6.6 to +5.2°C Tfm = none Tm_{ICE} = none Tm_{CLATH} = none Th = none Td = none Salinity = none CO_2 density = 0.9 – 0.97 g/cm^3	Vol.% CO_2 = 20 – 80 Tm_{CO_2} = -57.8 to -56.6°C Th_{CO_2} = 1.8 – 27.4°C Tfm = -36.2 to -13.2°C Tm_{ICE} = -9.3 to -1.2°C Tm_{CLATH} = 3.6°C Th = 366.6 – 389.9°C Td = 203.3 – 242.2°C Salinity = 2.1 – 13.2 wt% NaCl eq. CO_2 density = 0.75 – 0.91 g/cm^3 Bulk density = 0.91 – 1.08 g/cm^3	Vol.% CO_2 = 10 – 20 Tm_{CO_2} = -56.9 to -59.2°C Th_{CO_2} = 10.8 – 24.2°C Tfm = -54.4 to -29.8°C Tm_{ICE} = -23.1 to 0.0°C Tm_{CLATH} = none Th = 201.3 – 347.2°C Td = none Salinity = 0 – 15.9 wt% NaCl eq. CO_2 density = 0.76g/cm^3
	Fluid inclusions in Mo-type vein H_2O-salt-CO_2-solid	**Fluid inclusions in post-gold quartz vein** CO_2 -rich	**Late secondary fluid inclusions** H_2O-Salt
	Vol.% CO_2 = 10 – 45 Tm_{CO_2} = -81.4 to -58.6°C Th_{CO_2} = 19.5°C Tfm = -53.7 to -23.5°C Tm_{ICE} = -23.2 to -7.2°C Th = 153.1 – 347.1°C Td = none Salinity = 10.7 – 42 wt% NaCl eq. CO_2 density = 0.79 g/cm^3	Vol.% CO_2 = 20 – 100 Tm_{CO_2} = -58.8 to -56.9°C Th_{CO_2} = 7.1 – 23.6°C Tfm = none Tm_{ICE} = none Tm_{CLATH} = 5.0°C Th = 271.1 – 411.4°C Td = none Salinity = 9.0 wt% NaCl eq. CO_2 density = 0.74 – 0.89 gm/cm^3 Bulk density = 0.8 – 0.99 g/cm^3	Vw% = <5 – 15 Tfm = -81.1 to -38.2°C Tm_{ICE} = -34.0 to -5.7°C Th = 68.9 – 223.4°C Salinity = 8.8 – 33.5 wt% NaCl eq.

Figure 12 Synthesis of microthermometric data from the four main vein types in the Junction deposit. Tm_{CO2}, melting temperature of the carbonic phase; Th_{CO2}, homogenisation temperature of the vapour carbonic phase to the liquid carbonic phase; Tfm, temperature of first melt; Tm_{ICE}, final melting temperature of ice or hydrate; Tm_{CLATH}, melting temperature of the carbonic clathrate; Th, temperature of homogenisation; Td, temperature of decrepitation; Lw, liquid water; Vw, vapour water; Vc, vapour CO_2; Lc, liquid CO_2; S, daughter mineral (unspecified); NaCl, halite daughter mineral; CO_3, carbonate daughter mineral.

They are regularly <10 cm thick, but can be up to 25 cm wide. They are commonly filled with quartz, coarse-grained calcite crystals up to 3 cm long (with rare ankerite), randomly orientated biotite laths that are up to 1 cm long and coarse pyrrhotite crystals up to 3 cm long. Quartz grains are large (several micrometres to millimetres), clear and undeformed. The post-gold vein assemblage comprises less than 5% in abundance of all the vein types recorded in the Junction deposit. Alteration around these veins is negligible and no selvedges have been observed where they cross-cut the Junction Dolerite.

FLUID INCLUSIONS IN THE POST-GOLD QUARTZ VEINS

Post-gold quartz veins host vapour-dominated, CO_2-rich, H_2O-poor fluid inclusions. The fluid inclusions are tabular to slightly rounded in shape, with negative crystal shapes

also present. These fluid inclusions are typically <15 μm in size and occur as 3-D arrays, or less commonly along healed microfractures.

Setting and composition of late secondary fluid inclusions

Late secondary fluid inclusions are common in syn-gold quartz veins and post-gold quartz veins, but their apparent absence from pre-gold Mo-type quartz veins is probably due to the limited number of Mo-type quartz veins investigated. Late secondary fluid inclusions are aqueous-rich and are predominantly <8 μm, but may be up to 45 μm in size. Their shape is typically irregular (Figure 7f), but rounded and tabular shapes are also common. Late secondary fluid inclusions often contain one or more daughter minerals. Halite and calcite daughter

Table 2 Raman spectroscopic data for fluid inclusions hosted in syn-gold quartz–calcite shear and extensional veins.

Sample No.	CO_2	CH_4	Vapour (%)	Daughter minerals	Hydrates present
Shear veins					
15	85	15	85	Unidentifiable	–
15	87	13	75	Nahcolite	–
28	–	–	–	Calcite (?rhodochrosite)	–
37	100	0	95	–	–
37	100	0	25	–	$CaCl_2$
37	100	0	80	–	–
37	100	0	25	–	–
37	100	0	99	–	–
41	27	73	80	Siderite	Trace $CaCl_2$
84	93	7	60	Calcite (?rhodochrosite)	–
84	99	1	65	–	–
84	97	3	50	–	–
84	100	0	65	–	–
84	100	0	100	–	–
250	86	14	70	–	–
250	29	71	95	–	–
250	0	100	85	–	–
250	37	63	90	–	–
250	79	21	90	–	–
Extension veins					
43	97	3	40	–	–
43	87	13	45	–	–
43	81	19	65	–	NaCl
43	98	2	60	–	–
43	100	0	10	–	$MgCl_2.12H_2O$
43	100	0	10	–	$MgCl_2.12H_2O$
43	100	0	15	–	$MgCl_2.12H_2O$
105	99	1	70	–	–
105	98	2	95	–	–
105	98	2	50	Nahcolite	–
105	100	0	25	–	$CaCl_2$
105	99	1	80	–	–
229	56	44	50	–	–
229	32	68	50	Halite	NaCl
229	87	13	100	–	–
229	79	21	100	–	–
233	96	4	90	–	–
233	94	6	90	–	–
233	100	0	40	–	–
233	100	0	40	–	–
233	98	2	100	–	–
233	98	2	40	–	–

minerals were identified optically and by Raman spectroscopy.

Many late secondary fluid inclusions are optically similar to the syn-gold, Type-C, early secondary fluid inclusions. The late secondary fluid inclusions also occur along fluid-inclusion trails that cut across grain boundaries. However, late secondary fluid inclusion trails can often be traced across the entire doubly polished thick section. Based on this cross-cutting relationship they are younger than the Type-C fluid inclusions. Further, the presence of large and occasionally multiple daughter minerals together with the microthermometric behaviour of this fluid-inclusion type distinguish the late secondary fluid inclusions from the Type-C fluid inclusions.

FLUID-INCLUSION METHODS AND PROCEDURES

Fluid inclusions were observed in quartz, calcite and albite. However, only fluid inclusions in quartz were analysed, as those in the other minerals were usually too small (<3 μm) and the opacity and/or the refractive nature of these minerals preclude their use.

Twenty-seven doubly polished thin-sections (21 syn-gold quartz veins, four post-gold quartz veins and two Mo-type quartz veins) were used for microthermometric analysis and Raman spectroscopy.

Microthermometry was carried out on a Reynolds Fluid Inc. fluid-inclusion heating–freezing stage attached to a Leitz Wetzlar Sm Lux-POL binocular microscope using the

method described by Shepherd *et al.* (1985). Laser–Raman spectroscopy utilised a Microdil-28 laser–Raman microprobe at the Australian Geological Survey Organisation in Canberra, following the technique of Liu and Mernagh (1990).

RESULTS

The microthermometric results obtained from all of the fluid inclusions analysed are summarised in Figure 12.

Fluid inclusions in the pre-gold Mo-type quartz veins

CO_2 melting temperatures in fluid inclusions from the Mo-type quartz veins occur below the CO_2 invariant point of –56.6°C (Tm_{CO2}). Raman spectroscopy found that CH_4 is always present in these fluid inclusions and can account for Tm_{CO2} temperatures between –58.6°C and –81.4°C (Table 3).

Fluid inclusions in the Mo-type quartz veins have eutectic temperatures for ice ± hydrates (Tfm_{ICE}) that range from –53.7°C to –23.5°C. The majority begin to melt below –45°C indicating that $CaCl_2$ is the major solute present in solution along with Mg^{2+} and Na^+ (Shepherd *et al.* 1985; Davis *et al.* 1990). Raman microanalysis on these hydrates was not performed.

Final melt temperatures for the ice phase (Tm_{ICE}) in fluid inclusions that do not contain daughter minerals or

Table 2 (Cont.)

Sample No.	CO_2	CH_4	Vapour (%)	Daughter minerals	Hydrates present
236	100	0	100	–	–
236	100	0	90	–	–
236	100	0	100	–	–
236	100	0	100	–	–
240	100	0	100	–	–
240	99	1	100	–	–
240	100	0	100	–	–
240	99	1	90	–	–
240	99	1	100	–	–
243	100	0	100	–	–
243	100	0	25	Halite	NaCl
243	99	1	60	–	–
243	100	0	80	–	–
248	100	0	80	–	–
248	100	0	70	–	–
248	100	0	100	–	–
248	98	2	100	–	–
248	99	1	70	–	–
248	94	6	95	–	–
248	97	3	85	–	–
248	97	3	100	–	–
251	88	12	100	–	–
251	94	6	100	–	–
251	100	0	100	–	–
251	96	4	100	–	–
251	99	1	25	–	NaCl/$CaCl_2$
259	100	0	100	–	–
259	100	0	70	–	–
259	100	0	100	–	–

form CO_2 clathrates range from –23.2°C to –7.2°C, indicating a fluid salinity range from 10.73 to 24.83 wt% NaCl equivalent (Figure 13) (Bodnar 1993). Only one fluid inclusion formed a CO_2 clathrate during low-temperature microthermometry and melted at 5.0°C. Using the clathrate melting curves of Collins (1979), this temperature corresponds to a salinity of 9.0 wt% NaCl equivalent. In contrast, salinity estimates calculated from the dissolution temperature of two daughter minerals indicate a salinity of 41–42 wt% NaCl equivalent (Figure 13) (Shepherd *et al.* 1985).

Ten fluid inclusions in the Mo-type quartz veins homogenised into the liquid phase (Th) between 153.1°C and 347.1°C (Figure 13). No pressure correction was applied to these values because an estimate of the pressure of entrapment could not be calculated. Two halite-bearing fluid inclusions in the Mo-type quartz veins homogenised by dissolution of the daughter minerals (Ts_{NaCl}) at 339.8°C and 347.1°C (Figure 13). The dissolution temperature of the daughter minerals was higher than the disappearance temperature of the vapour phase in these fluid inclusions.

Fluid inclusions in syn-gold quartz–calcite veins

On warming, solid CO_2 melts to a liquid phase and a vapour phase close to its invariant point of –56.6°C. Tm_{CO2} values for the Type-A and Type-B fluid inclusions range from –56.6°C to –62.1°C (Figure 14). Raman spectroscopy shows that the vapour phase in most syn-gold fluid inclusions is dominated by CO_2. However, CH_4 is common and would account for Tm_{CO2} excursions below –56.6°C (Table 2). No N_2 was detected in these veins during Raman analysis.

Tfm_{ICE} for Type-B and Type-C fluid inclusions are widely distributed (–61.5°C to –13.2°C), indicating the presence of K^+ and/or Mg^{2+} and/or Ca^{2+} together with Na^+ in the solution (Shepherd *et al.* 1985). However, most Tfm_{ICE} values are between –35°C and –20°C. Low-temperature Raman spectroscopy reveals that the solute chemistry of individual fluid inclusions can be variable and complex and three hydrate species ($NaCl.2H_2O$, $CaCl_2.6H_2O$ and $MgCl_2.12H_2O$) were found to exist in the syn-gold fluid inclusions (Table 2). Tfm_{ICE} data and Raman analysis indicate that $Na^+ >> Mg^{2+} > Ca^{2+}$. Raman analysis detected strong $NaCl.2H_2O$ signals in fluid-inclusion hydrates, but only moderate $MgCl_2.12H_2O$ signals and broad $CaCl_2.6H_2O$ peaks. No K^+ hydrates were identified by Raman spectroscopy. Daughter minerals other than halite that were present in the syn-gold fluid inclusions were identified by Raman spectroscopy to be calcite and/or

rhodochrosite, siderite and nahcolite (Table 2). Type-A fluid inclusions did not produce any low-temperature solute data.

Tm_{ICE} values for Type-B fluid inclusions that did not form a clathrate on cooling range from –0.8 to –13.2°C. Salinity estimates calculated from these fluid inclusions range from 1.4 to 17.1 wt% NaCl equivalent (Bodnar 1993) (Figure 15). However, the mean salinity value is 8.8 wt% NaCl equivalent. Tm_{ICE} data for Type-C fluid inclusions range from 0 to –12.0°C. These values equate to fluid salinity estimates that range from 0 to 15.9 wt% NaCl equivalent (mean = 8.2 wt% NaCl equivalent: Figure 15). Salinity estimates were also calculated from the melting temperature of pure CO_2 clathrates using the clathrate melting curves of Collins (1979). Clathrate melting points (Tm_{CLATH}) cluster between 2.8°C and 6.9°C. These temperatures correspond to salinity estimates ranging from 6.2 to 12.1 wt% NaCl equivalent, with a mean total salinity at 8.1 wt% NaCl equivalent (Figure 15).

Homogenisation temperatures for pure CO_2 (Th_{CO2}) range from –6.6°C to 30.1°C. Homogenisation is always into the liquid state. $XCH_4/(CO_2 + CH_4)$ estimates calculated from coexisting Tm_{CO2} and Th_{CO2} data using the method of Jacobs and Kerrick (1981) show that the vapour phase in the syn-gold fluid inclusions ranges from 0 to 21 mol% CH_4. These estimates are comparable to the qualitative results obtained by Raman spectroscopy, which reveal that syn-gold fluid inclusions contain between 0 and 100 mol% CH_4 in the
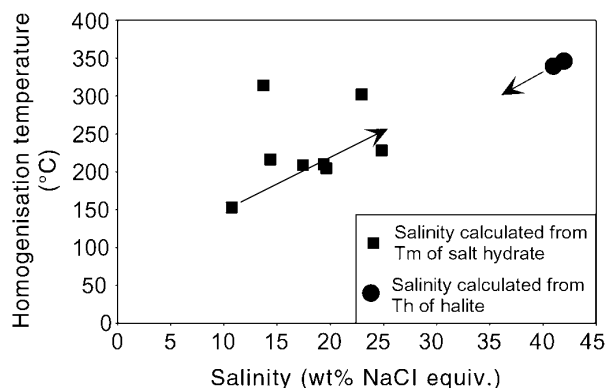

Figure 13 Temperature *vs* salinity plot for fluid inclusions hosted by the Mo-type quartz veins. The arrows are to indicate a subtle trend that suggests that these veins precipitated when a moderately hot, moderately saline fluid mixed with a hot, highly saline fluid.

Table 3 Raman spectroscopic data for fluid inclusions in Mo-type quartz veins.

Sample No.	CO_2	CH_4	Vapour (%)	Daughter minerals
Pseudoprimary inclusion				
66	25	75	40	Halite/unidentified carbonate
66	36	64	35	Halite
66	37	63	25	–
66	74	26	65	–
66	60	40	50	Halite
66	81	19	50	Halite/unidentified carbonate

vapour phase, with the majority containing <2 mol% CH_4 (Table 4).

An important fact highlighted by Raman spectroscopy is that CH_4-rich (>10 mol% CH_4) and CH_4-dominated (>50 mol% CH_4) fluid inclusions are found in quartz grains that occur near vein tips and within, but adjacent to, the margin of the vein where calcite–albite alteration dominates (Figure 8b). Type-A and Type-B fluid inclusions that occur in quartz grains distant from the vein margin are almost exclusively pure CO_2, or CO_2-rich. This finding suggests that CO_2:CH_4 ratios in fluid inclusions are zoned with respect to the vein margins.

Total homogenisation of Type-B and Type-C fluid inclusions in the syn-gold quartz veins occurs by the disappearance of the liquid into the vapour phase or by the disappearance of the vapour into the liquid phase between 201.3°C and 389.9°C (Figure 16). All of the Type-A fluid inclusions analysed were essentially monophase vapour-only fluid inclusions and no Th values were recorded. Many fluid inclusions decrepitate prior to homogenisation. Decrepitation (Td) usually occurred in the vapour-rich fluid inclusions, but also occurred in fluid inclusions with only 20 vol% vapour. It can be assumed that Td is the minimum temperature of entrapment for these fluid inclusions.
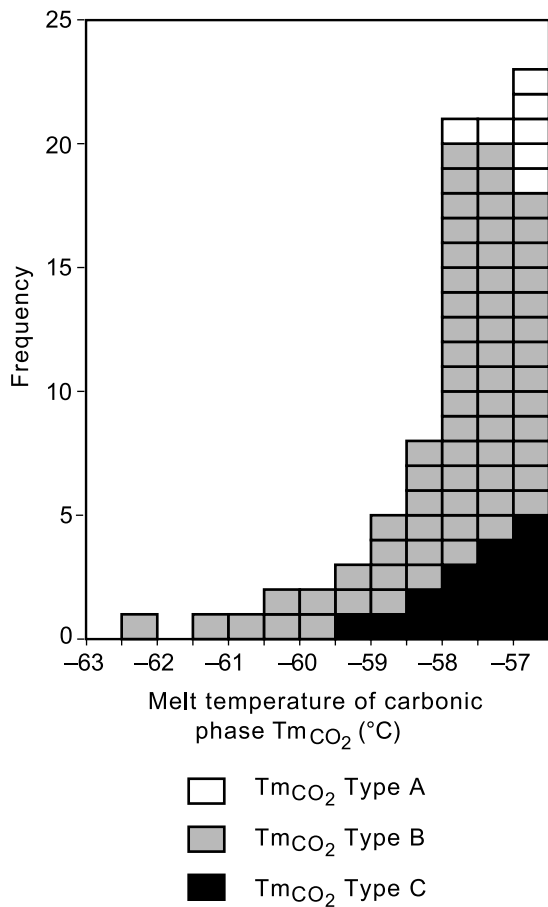
Type-B fluid inclusions with vapour to water ratios >50 vol% often decrepitated before homogenisation was reached. Twenty-four of 66 Type-B fluid inclusions decrepitated between 188.9°C and 311.2°C. Total homogenisation into the liquid phase occurs between 223.0°C and 389.9°C: total homogenisation into the vapour phase concurs with these values, occurring between 213.1°C and 373.0°C (Figure 16).

Type-C fluid inclusions have a similar Th range to the Type-B fluid inclusions. No Type-C fluid inclusions decrepitated during heating. Most Type-C fluid inclusions homogenise into the liquid phase between 205.2°C and 373.8°C. Other Type-C fluid inclusions homogenise into the vapour phase between 201.3°C and 300.4°C (Figure 16).

Bulk fluid-inclusion densities were calculated for the two-phase Type-B fluid inclusions. Using the equations of state relative to the H_2O–CO_2–CH_4–NaCl system of Jacobs and Kerrick 1981), the range of fluid densities for this fluid-inclusion type range from 0.91 to 1.08 g/cm^3.

Pressure estimates were calculated for Type-B fluid inclusions using the equation of state relative to the H_2O–CO_2–CH_4–NaCl system of Jacobs and Kerrick (1981) adopted in the MacFlinCor program (Brown & Hagemann 1995). Assuming no post-trapping modifications, the fluid inclusions indicate that entrapment occurred at pressures between 77 MPa and 444 MPa. Most fluid inclusions indicate pressures between 130 MPa and 290 MPa.

Figure 14 Frequency histogram of Tm_{CO_2} for Type-A, B, and C fluid inclusions from either shear or extensional syn-gold quartz–calcite veins. Each square represents one fluid-inclusion analysis.
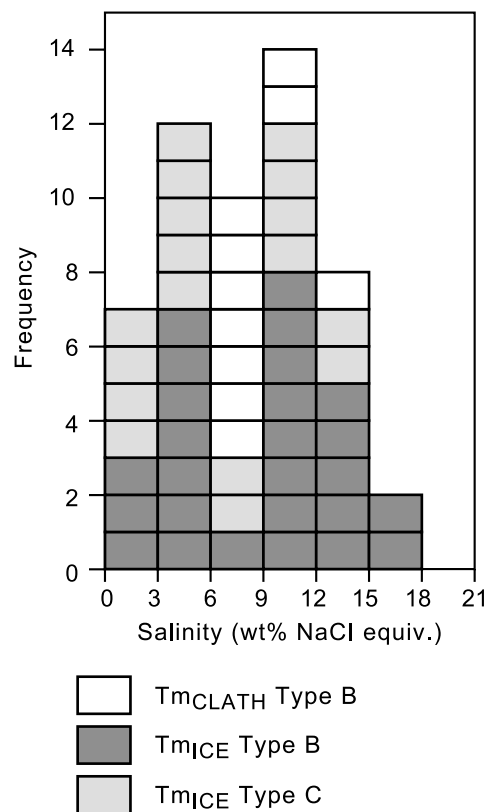

Figure 15 Frequency histogram showing the salinity estimates in wt% NaCl equivalent calculated from Tm_{ICE} and Tm_{CLATH} for Type-B and Type-C fluid inclusions found in syn-gold quartz–calcite veins. Each square represents one fluid-inclusion analysis.

Fluid inclusions in the post-gold quartz veins

Twelve fluid inclusions from three post-gold quartz veins were analysed by microthermometry. Tm_{CO_2} values range from –58.8°C to –56.9°C, indicating that they are CO_2-dominated fluid inclusions. Raman spectroscopy shows that the vapour phase in most post-gold fluid inclusions is pure CO_2 (Table 4). The vapour phase in eight fluid inclusions analysed by Raman spectroscopy in two post-gold quartz veins contained 99–100 mol% CO_2. However, the vapour phase in five fluid inclusions in a different post-gold quartz vein contained between 17 and 43 mol% CH_4 (Table 4). The presence of CH_4 would account for Tm_{CO_2} values below –56.6°C. No N_2 was detected in these veins during Raman analysis. Zonation of CO_2:CH_4 ratios with these fluid inclusions with relation to the vein – wall-rock margin was not observed.

No fluid inclusions in the post-gold quartz veins formed ice or hydrates on cooling. Therefore no Tfm or Tm data were recorded. However, one post-gold fluid inclusion formed a CO_2 clathrate that melted at +5.0°C. This indicates a fluid with a salinity of 9 wt% NaCl equivalent.

CO_2 liquid in the CO_2-rich fluid inclusions homogenised into the liquid state between 7.1°C and 23.6°C. Total homogenisation temperatures for most post-gold fluid inclusions range from 271.1°C to 313.2°C. One fluid inclusion homogenised at 411.4°C. Homogenisation was into the vapour phase in all cases.

Late secondary fluid inclusions

Late secondary fluid inclusions do not contain CO_2 or CH_4. Microthermometric observations and Raman spectroscopy confirm this. Tfm_{ICE} values range from –81.1°C to –38.2°C.

Most of the values range between –65°C and –40°C. These temperatures indicate that Ca^{2+} is a dominant ion present in these fluid inclusions, along with Na^+ (Shepherd *et al*. 1985). Low-temperature Raman spectroscopy confirms that $NaCl.2H_2O$ and $CaCl_2.6H_2O$ are present in these fluid inclusions and that $CaCl_2$ dominates over NaCl (Table 4). However, neither $MgCl_2$ nor KCl were detected. Tm_{ICE} data range from –34.0°C to –5.7°C. Salinity estimates calculated from these fluid inclusions range from 8.81 to 31.99 wt% NaCl equivalent (Figure 17) (Bodnar 1993).

Homogenisation of the vapour into the liquid phase occurred between 68.9°C and 215.9°C, whereas homogenisation by dissolution of halite occurred between 118.9°C and 223.4°C (Figure 17). Salinity estimates calculated from the dissolution temperature of 15 daughter minerals range from 28.4 to 33.5 wt% NaCl equivalent. This range is in reasonable agreement with the higher salinity estimates calculated from Tm_{ICE} values obtained from the late secondary fluid inclusions that did not contain daughter minerals (Figure 17).

DISCUSSION

Interpretation of fluid-inclusion results

Thermometric and Raman data support geological observations that four different fluid events (Mo-type, syn-gold, post-gold and late secondary) are trapped in fluid inclusions in three different vein systems. Further, Raman spectroscopy confirms the presence of CO_2 and/or CH_4 in most of the fluid inclusions, and $NaCl.2H_2O$, $CaCl_2.6H_2O$ and $MgCl_2.12H_2O$ in some of the fluid inclusions from all vein types sampled at Junction.

Table 4 Raman spectroscopic data for fluid inclusions hosted in post-gold quartz veins and secondary fluid inclusions hosted in a syn-gold quartz–calcite shear vein.

Sample No.	CO_2	CH_4	Vapour (%)	Daughter minerals	Hydrates present
Pseudosecondary inclusion, post-gold quartz vein					
93	57	43	80	–	–
93	62	38	90	–	–
93	83	17	95	–	–
93	62	38	40	–	–
93	69	31	65	–	–
131	100	0	100	–	–
131	100	0	95	–	–
131	100	0	80	–	–
131	100	0	100	–	–
131	99	1	100	–	–
136	100	0	100	–	–
136	100	0	100	–	–
136	100	0	100	–	–
Late secondary inclusion, syn-gold quartz–calcite shear vein					
41	–	–	<5	Halite/calcite (?rhodochrosite)	NaCl
41	–	–	<5	Halite/calcite (?rhodochrosite)	$CaCl_2$/NaCl
41	–	–	<5	Halite/calcite (?rhodochrosite)	$CaCl_2$

Geological evidence shows that a hot, moderately to highly saline fluid that contained both CO_2 and CH_4 intruded the Junction Dolerite prior to the gold-mineralising event and precipitated the molybdenite-bearing quartz veins. Raman analysis and Tm_{CO_2} values as low as $-81.4°C$ indicate that CH_4 was a significant constituent in the Mo-bearing fluid (Shepherd *et al.* 1985). Fluid salinity estimates and homogenisation temperatures for the Mo-type fluid inclusions are highly variable (10.73–42 wt% NaCl equivalent and 153.1–347.1°C). However, Mo-type fluid inclusions, with their consistent vapour to liquid ratios, do not indicate that boiling or fluid unmixing occurred.

No pressure correction was applied to the homogenisation values obtained from the Mo-type fluid inclusions, because an estimate of the pressure of entrapment could not be calculated. The limited and uncorrected data appear to reveal a transgressive trend in Figure 13. Given that boiling or fluid unmixing are not evident, it is proposed that any pressure correction that needed to be applied

would be consistent for all of the Mo-type fluid inclusions and the trend seen in Figure 13 would not be effected. The interpretation that a transgressive trend exists is given with caution. Ideally, more data points could validate or refute this speculation. However, if the trend is real, it suggests that a hot, highly saline fluid capable of precipitating halite mixed with a cooler, less saline fluid to precipitate the Mo-type quartz veins. This interpretation is supported by the fact that halite-bearing fluid inclusions generally occur together in small populations (Figure 7a) and do not occur with fluid inclusions without halite daughter minerals. Mixing trends are frequently encountered in studies of convectively driven hydrothermal fluid circulation in and around intrusive bodies (Shepherd *et al.* 1985). Therefore, although the extent of convection is unknown, it is possible that the Mo-type quartz veins precipitated from fluids that originated from the dewatering of the felsic, porphyry dykes that intruded the Junction Dolerite around the time of peak metamorphism. Given that the porphyry dykes are limited to the upper levels of the deposit (Figure 3), this interpretation explains why the Mo-type quartz veins are also restricted to the upper levels of the deposit.

Syn-gold quartz veins at Junction host three optically different fluid-inclusion types—CO_2-dominated, H_2O–CO_2-dominated, and H_2O-dominated—consistent with results reported from similar orogenic lode-gold deposits (Robert & Kelly 1987; Clark *et al.* 1989; Ho *et al.* 1990a; Robert *et al.* 1995). The three fluid-inclusion types identified at Junction probably evolved from a single parent ore fluid. Coexisting CO_2-dominated and H_2O-dominated fluid inclusions are considered by Robert and Kelly (1987) and Robert *et al.* (1995) to result from variable degrees of intermittent unmixing from a homogeneous parent H_2O–CO_2 fluid of low salinity. Total homogenisation of Type-B and Type-C fluid inclusions into the liquid and vapour phase over the same temperature range in some syn-gold quartz veins supports this interpretation and indicates that fluid unmixing was due to fluid immiscibility induced by pressure related boiling/effervescence. In this case, fluid immiscibility was triggered by fluctuations in fluid pressures between lithostatic and lower values associated with seismic rupture along the Junction shear zone during vein development (Sibson *et al.* 1988; Robert *et al.* 1995). The presence of free
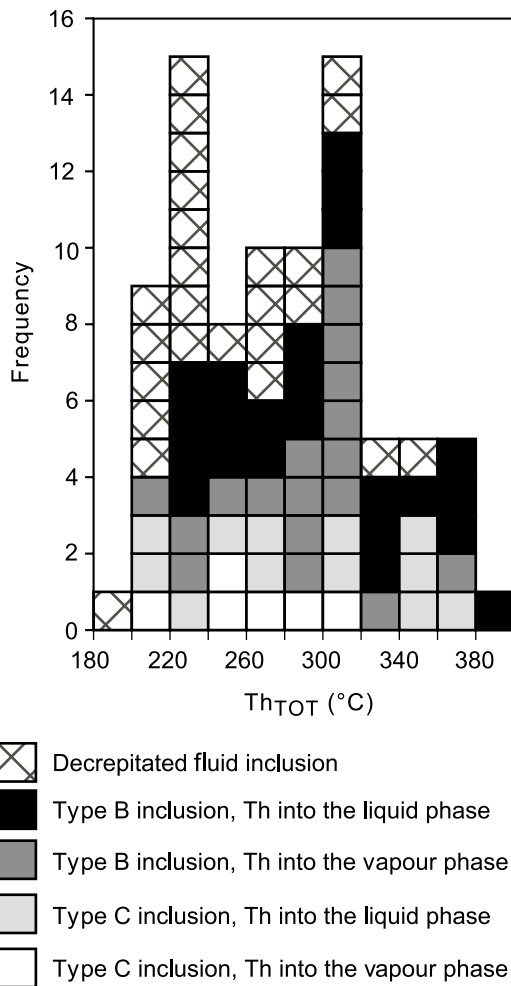

Figure 16 Homogenisation and decrepitation temperatures for all Type-B and Type-C fluid inclusions hosted in the syn-gold quartz–calcite veins. Each square represents one fluid-inclusion analysis.
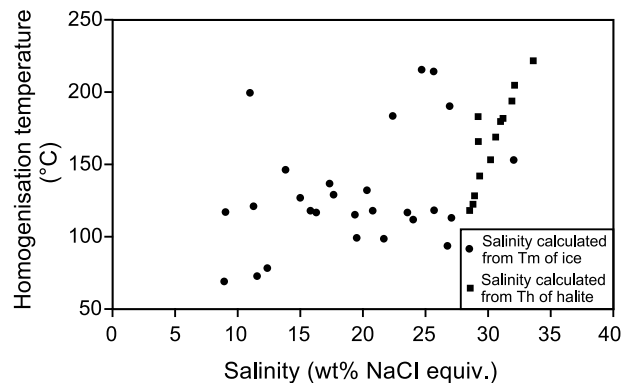

Figure 17 Temperature *vs* salinity plot for the late secondary fluid inclusions. Almost all of these fluid inclusions homogenise below 200°C and have moderate to very high salinities.

gold in some veins throughout the deposit supports the interpretation that phase separation / fluid unmixing occurred (Robert & Kelly 1987; Hagemann & Cassidy 2000).

The fact that fluid unmixing occurred explains the spread in the salinity estimates calculated from Tm_{ICE} and Tm_{CLATH} values from syn-gold fluid inclusions. The mean salinity of the syn-gold fluid inclusions approximates 8 wt% NaCl equivalent using either Tm_{ICE} or Tm_{CLATH}. The salinity estimates from syn-gold fluid inclusions at the nearby Victory gold mine, approximately 15 km north of Junction, concur with our data, ranging from 8.0 to 9.5 wt% NaCl equivalent (Clark *et al.* 1989). However, salinity estimates above 8 and up to 17.08 wt% NaCl equivalent are common at Junction, and halite daughter minerals have been identified. The production of a high-salinity fluid from a relatively low-salinity H_2O-CO_2 fluid is possible when unmixing occurs (Bowers & Helgeson 1983b; Shepherd *et al.* 1985). Therefore, salinity values up to 17.08 wt% NaCl equivalent at Junction are probably a process of fluid solutes being concentrated into H_2O-dominated, Type-C fluid inclusions at the same time as CO_2 was partitioned into the CO_2-dominated, Type-A fluid inclusions.

The detection of $NaCl.2H_2O$, $MgCl_2.12H_2O$ and $CaCl_2.6H_2O$ by Raman spectroscopy corresponds to Tfm values that cluster between $-30°C$ and $-47°C$. Further, mixed $H_2O-Ca-Na-Mg-Cl$ solutions interpreted from eutectic temperatures that fall between $-35°C$ and $-61.5°C$ are supported by Raman spectroscopy that detected both $NaCl.2H_2O$ and $CaCl_2.6H_2O$ in at least one fluid inclusion (Table 3).

Homogenisation temperatures for syn-gold fluid inclusions range from $205.2°C$ to $389.9°C$. However, it is unlikely that the ambient wall-rock temperature varied significantly during vein development (Robert *et al.* 1995). Instead, fluid pressure fluctuations at the time of entrapment can account for most of the observed data scatter. The presence of NaCl and other solutes that may be present in the fluid inclusions may also lead to variations in homogenisation temperatures (Takenouchi & Kennedy 1965; Bowers & Helgeson 1983a). Further, the addition of CH_4 to the H_2O-CO_2 system generally raises the internal pressure in a fluid inclusion and leads to a lowering of Th (Duan *et al.* 1992a, b). Stable isotope geothermometry and mineral equilibria thermodynamic calculations indicate that the homogenisation temperatures of most fluid inclusions is probably at or below the ambient temperature calculated for the Junction shear zone at the time of mineralisation. The majority of formation temperatures calculated by oxygen isotope geothermometry occur between $381°C$ and

$434°C$. This temperature range is in agreement with mineral equilibria thermodynamic calculations for gold mineralisation associated with a biotite–calcite–quartz–albite–pyrrhotite ± pyrite alteration assemblage in mafic host rocks (Witt *et al.* 1997). Therefore, we conclude that gold mineralisation occurred at approximately $400°C$.

Implication of anomalous CH_4 volumes in syn-gold fluid inclusions

The identification by Raman spectroscopy that some fluid inclusions contain anomalous CH_4 volumes is in agreement with workers who have detected significant CH_4 in other Archaean lode-gold deposits. Other Yilgarn gold deposits that contain pure CH_4 fluid inclusions include Oroya (Ho 1987), Lancefield (Ho *et al.* 1992), Wiluna (Hagemann *et al.* 1996), Mt Charlotte (Ho *et al.* 1990a; Mernagh 1996) and Golden Kilometre (Gebre-Mariam *et al.* 1997). Some of these deposits have graphitic wall rocks (e.g. Lancefield), whereas others occur adjacent to or in carbonaceous sediments (e.g. Oroya). In contrast, Mt Charlotte mineralisation at Kalgoorlie occurs within the granophyric unit of the Golden Mile Dolerite and contains quartz veins hosting $H_2O-NaCl-CO_2-CH_4$ fluid inclusions including fluid inclusions with up to 50 mol% CH_4 (Ho 1987; Ho *et al.* 1990a; Mernagh 1996). Clearly, deposits such as Junction and Mt Charlotte do not have a one-to-one correspondence with carbonaceous host rocks and an alternative explanation is needed.

Preliminary Raman results from Junction showed that fluid inclusions with up to 100 mol% CH_4 in the vapour phase occurred in quartz grains found in samples that are dominated by an albite–calcite–chlorite>quartz>biotite>pyrrhotite assemblage (samples 41 and 229; Table 2). These samples are vein-tip samples that grade into quartz-dominated veins as the vein thickens beyond 1–2 cm. Alternatively, sample 250 contains free gold in quartz and calcite and the CH_4-rich fluid inclusions are hosted adjacent to the calcite–gold mineralisation. Other syn-gold vein samples that are dominated by quartz, host fluid inclusions that have pure CO_2 or contain only trace amounts of CH_4 in the vapour phase (Table 2). The vein-tip samples suggested that CH_4-bearing fluid inclusions are associated with the alteration assemblage that occurs at the vein margin or, in the case of sample 250, with free gold. Phase separation has been suggested as an important mechanism for depositing free gold and producing CO_2-rich and CH_4-rich fluid inclusions (Hagemann & Cassidy 2000).
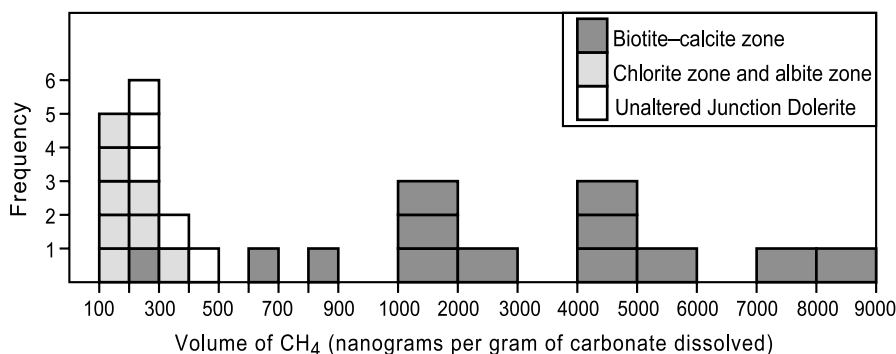

Figure 18 Histogram showing the volumes of CH_4 in vein and matrix carbonate samples (carbonate not specified) collected from the mineralised, altered and unaltered Junction Dolerite. Note the change in scale between 900 ng/g and 1000 ng/g carbonate dissolved.

However, samples 41 and 229 are not associated with visible or microscopic free gold. Therefore, their proximity to the intense wall-rock alteration assemblage prompted a further investigation.

Follow-up investigations were performed on vein samples that had albite–calcite–chlorite>quartz ± biotite ± pyrrhotite at the vein margin, but graded into mono-mineralic quartz toward the centre of the vein (Figure 8a). There is no free gold evident in these samples. Raman results from samples 15, 43 and 251 confirmed that fluid inclusions hosted in quartz grains, which coexist with albite, calcite, chlorite ± pyrrhotite near the vein margin, contain elevated CH_4 volumes in the vapour phase. The vapour phase in fluid inclusions hosted in quartz grains found toward the centre of the same vein contain >98 mol% CO_2 (Table 2). In contrast, some syn-gold veins with the same albite, calcite, chlorite ± pyrrhotite alteration assemblage at the vein margin did not contain appreciable CH_4, and no zonation was apparent in these samples. Nevertheless, the results indicate that CO_2:CH_4 ratios in fluid inclusions are zoned with respect to the vein wall-rock margin in at least half of the syn-gold veins that had albite–calcite–chlorite>quartz ± biotite ± pyrrhotite occurring at the vein margin. These findings are unlike the results obtained from fluid inclusions hosted in the Mo-type quartz veins or the post-gold quartz veins in which CH_4 volumes were either negligible or elevated across the entire doubly polished thick section used for the fluid-inclusion study.

The finding that CO_2:CH_4 ratios in fluid inclusions are zoned with respect to the vein wall-rock margin in the syn-gold quartz veins is rarely reported. The closest analogy comes from the Hollinger–McIntyre deposit in Canada, where elevated CH_4 volumes, and thus lower CO_2:CH_4 ratios, occur in scheelite at the margins of gold quartz veins and contrast with higher CO_2:CH_4 ratios detected in the quartz collected from the centre of the same gold-bearing veins (Bray *et al*. 1991; Bray & Spooner 1992). At Junction, syn-gold, vein calcite collected from the margin of selected quartz veins in the biotite–calcite zone is known to contain high CH_4 and ethane volumes (up to 8067 ng CH_4 and 51 ng of ethane per gram of dissolved calcite (Figure 18) (Polito 1999). However, these gases were liberated from the sample by dissolving the carbonate fraction of the whole rock in a near-neutral solution of ethyl diamine tetra-acetic acid and then analysing the gas by gas chromatography (Ferguson 1987; Polito 1999). Light hydro-carbons cannot be liberated from quartz using this tech-nique, therefore, the hydrocarbon content in the carbonate cannot be compared with the hydrocarbon content in the coexisting quartz. Nevertheless, it is worthwhile noting that syn-gold, vein calcite collected from the chlorite zone and the albite zone contains <460 ng CH_4/g of dissolved calcite and no ethane (Figure 18) (Polito 1999). In effect, the CH_4 is restricted to the biotite–calcite zone in the Junction shear zone, suggesting that CH_4 and ethane may not travel as part of the ore-forming solution (see below for further discussion).

On the origin of the CH_4, fluids above 400°C can trans-port significant volumes of CH_4 as a soluble phase in solu-tion (Duan *et al*. 1992b). Therefore, the CH_4-bearing fluid could have originated from a deep crustal source. Further,

CH_4 contents in CO_2-rich fluids arising from high-grade metamorphic devolatilisation can exceed approximately 0.2 mol% if graphite or appreciable volumes of water at relatively low P–T–f_{O2} are present (Hall & Bodnar 1990). Graphite is known to occur in the metasedimentary Black Flag Group, the unit of rock intruded by the Junction Dolerite. Thus, it is possible that CH_4 was present as either a soluble phase in the ore solution or generated in the Black Flag Group or similar during the ascension of the gold-bearing hydrothermal fluid.

Fluid unmixing experiments show that CH_4 has a large immiscibility field and only small (<5 mol%) amounts of CH_4 are soluble in aqueous brines up to 300 MPa and 400°C (Naden & Shepherd 1989). Although temperatures are unlikely to have varied, pressure fluctuations from 77 MPa to 444 MPa would have been the ideal trigger needed to initiate fluid unmixing and produce CH_4-rich fluid inclu-sions. The restricted solubility of CH_4 in an aqueous brine suggests that very little fluid – wall–rock interaction is required to produce CH_4-rich fluid inclusions (Naden & Shepherd 1989). However, the problem here is that fluid unmixing not only fails to adequately explain the zonation of CO_2:CH_4 ratios detected across the quartz–calcite veins, but it also fails to explain the relative absence of CH_4 in the calcite phase of the quartz–calcite veins that extend into the chlorite zone and the albite zone (Figure 18). If CH_4 was present in the gold-carrying fluid, then elevated CH_4 volumes should be detectable across the entire width of the quartz vein and it should be present in the calcite that is present in syn-gold quartz–calcite veins, which extend into the chlorite zone and the albite zone.

If fluid unmixing did not produce the observed results, then coexisting CH_4-rich and CO_2-rich fluid inclusions could be a function of post-entrapment alteration. Both physical and chemical processes are known to alter fluid-inclusion compositions after initial entrapment. Methane can be concentrated into some fluid inclusions during rupturing and resealing of existing fluid inclusions as one or more fluid components are selectively lost or gained during post-entrapment recrystallisation (Hall & Bodnar 1990; Van den Kerkhof *et al*. 1991). Similarly, CH_4 can be formed *in situ* by the introduction of H^+ when f_{H2} and f_{O2} outside and inside the fluid inclusion are different (Mavrogenes & Bodnar 1994). However, neither mechanism adequately explains why CH_4-rich fluid inclusions are more common at the margin of quartz–calcite veins and rare at the centre of the same vein in which CO_2-rich fluid inclusions predominate.

Based on the fact that CO_2:CH_4 ratios are zoned across the quartz veins at Junction and that fluid unmixing, post-entrapment recrystallisation and component addition/loss inadequately explains this observation, it is concluded that the CO_2-rich, gold-carrying fluid contained little or only trace CH_4. Low-temperature microthermometry and Raman analyses support this interpretation. They show that the majority of fluid inclusions are dominated by CO_2 and comparatively few contain anomalous CH_4. If fluid unmixing or post-entrapment recrystallisation and com-ponent addition/loss did occur, then more fluid inclusions should contain anomalous CH_4 volumes and Th_{CO2} values may be expected to show even a slight bimodal distribution, but clearly they do not (Figure 14).

Incremental vein growth highlighted by growth layering that incorporates parts of the wall rock into the vein structure (Figure 9b) indicates that the youngest vein material is often located at the margins of the quartz–calcite veins (Boullier & Robert 1992; Robert *et al.* 1994, 1995). Given that elevated CH_4 volumes are only detected at the margins of the quartz–calcite veins, we propose that CH_4 was either introduced during the later stages of gold deposition or was produced late, but *in situ* by the reduction of CO_2 during its interaction with the Fe-rich Junction Dolerite. Neither of these two methods of CH_4 introduction rely exclusively on fluid unmixing of a CH_4-bearing auriferous fluid or post-entrapment alteration to explain the zonation of CO_2:CH_4 ratios in fluid inclusions across the quartz–calcite veins.

If the CH_4 was introduced from an external source after gold deposition, then foliation within the Junction shear zone could have provided a pathway for the fluid to travel along before being trapped in quartz- and calcite-hosted fluid inclusions at the vein margins. The fluids trapped in the late secondary fluid inclusions do not contain any carbonic fluids and could not have been the source for the CH_4. However, the post-gold quartz veins, known to host vapour-dominated, CH_4-rich and CO_2-rich fluid inclusions are an obvious CH_4 source. Although microthermometric analysis failed to detect anomalous CH_4 in the post-gold quartz veins, Raman spectroscopy found that CH_4 is common in some post-gold quartz veins.

If the post-gold veining event or similar did introduce CH_4 to the Junction shear zone, then this fluid should have affected the $\delta^{18}O$ values of the syn-gold quartz or calcite, or both. Homogenisation temperatures for the post-gold quartz veins predominantly cluster between 271.1°C and 313.2°C. This temperature range is marginally lower than, but in agreement with, formation temperatures ranging from 289°C to 359°C, calculated by oxygen isotope geothermometry for three coexisting hydrothermal quartz and calcite post-gold quartz vein samples (Table 1) (Polito 1999). Both methods indicate that the post-gold quartz veins formed at approximately 310°C ± 30°C. The post-gold quartz vein temperatures are in disagreement with the formation temperatures calculated by mineral equilibria thermodynamic calculations for the syn-gold alteration assemblage and most of the formation temperatures calculated from oxygen isotope geothermometry formed on quartz–calcite veins in the biotite–calcite zone. Four of the ten formation temperatures calculated by oxygen isotope geothermometry for the syn-gold quartz–calcite vein samples indicate precipitation between 289°C and 339°C, a range that overlaps the formation temperature calculated for the post-gold quartz veins. This may be evidence for the late introduction of a CH_4-bearing fluid associated with the post-gold quartz veins. However, the lower temperatures obtained from the syn-gold quartz–calcite veins may simply be indicating a decreasing temperature regime as activity on the Junction shear zone came to an end. Alternatively, it is also possible that some of the syn-gold quartz and calcite pairs are in disequilibrium with each other due to an unrelated geothermal event. Oxygen isotope disequilibrium is a frequently noted problem when using quartz and carbonate pairs for geothermometry in orogenic lode-gold deposits (Colvine *et al.* 1988) in which late vein systems are not described and presumably do not exist. Therefore, although the low-temperature estimates from

the biotite–calcite zone overlap the formation temperature range calculated for the post-gold quartz veins, the evidence for overprinting by a later, cooler, CH_4-bearing fluid is inconclusive.

The proximity of the CH_4-rich fluid inclusions to the vein margin, plus the anomalous CH_4 and ethane volumes within vein calcite in the biotite–calcite zone, indicates that a relationship exists between the biotite–calcite zone and CH_4. If the post-gold veining event or similar did introduce CH_4 into the Junction shear zone, then the comparatively low volumes of CH_4 detected in the vein calcite collected from the chlorite zone or the albite zone remain unexplained (Figure 18). The chlorite zone, like the inner biotite–calcite zone, has a well to moderately developed foliation. By contrast, the albite zone rarely has a weakly developed foliation. Nevertheless, if a CH_4-bearing fluid did travel along the well-developed foliation that is present in the inner biotite–calcite zone, then it is not unreasonable to expect the same fluid to travel along the foliation present in the chlorite zone or the albite zone before being trapped at the vein margins in these zones. Therefore, it is reasonable to investigate the possibility that the CH_4 and traces of ethane were a by-product of a hot H_2O–CO_2 fluid interacting with an iron-rich host rock in a reduced environment. The reduction of CO_2 to CH_4 in a reduced environment is proposed to explain the variation and zonation of $\delta^{13}C$ values of carbonates in other Archaean lode-gold deposits, including Mt Charlotte (Colvine *et al.* 1988; Golding *et al.* 1990).

Geological and geochemical data show that the Junction shear zone was at or below the pyrite–pyrrhotite–magnetite and CO_2(aq)–CH_4(aq) buffers in the biotite–calcite zone. The predominance of pyrrhotite over pyrite in an upper greenschist facies alteration assemblage indicates that reduced conditions prevailed in the biotite–calcite zone (Mikucki & Ridley 1993). CO_2 was present in sufficient quantities in the gold-bearing fluid and H_2 could be derived from a number of sources including H_2O and any of the $AuHS(H_2S)_3^0$, $Au(HS)_2^-$ or $Au(HS)^0$ complexes. Mikucki (1998) reported that gold deposition is thought to occur during the interaction of S-rich fluids and Fe-bearing host rocks by the coupled reactions:

$$FeO\ rock + 2H_2S^0 = FeS_{(Po)} + H_2O + H_2(g) \qquad (1)$$

and

$$Au(HS)_2^- + H^+ + 1/2H_2(g) = Au + 2H_2S^0 \qquad (2)$$
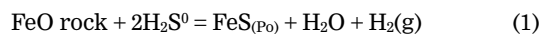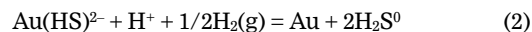
The presence of free hydrogen then allows CH_4 plus other light hydrocarbons to form by the disequilibrium reactions:

$$nCO + (2n+1)H_2 = C_nH_{(2n+2)} + nH_2O \qquad (3)$$

$$nCO_2 + (3n+1)H_2 = C_nH_{(2n+2)} + nH_2O \qquad (4)$$
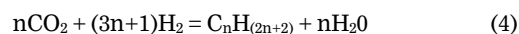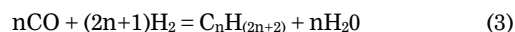
The overall reaction may not be too dissimilar from Fischer–Tropsch type synthesis. Fischer–Tropsch type synthesis of light hydrocarbons requires a reduced environment, a CO_2-rich fluid, hydrogen, and a Group VIII metal (e.g. iron) in its native or oxide form as a catalyst (Anderson 1984; Salvi & Williams-Jones 1997). The process can occur naturally in the presence of wustite or magnetite (Anderson 1984). The potential to generate CH_4 and other low molecular weight, light hydrocarbon chains, such as ethane, is a function of temperature,

pressure and H_2 to C ratios. The shorter chains are always favoured at higher temperatures (Salvi & Williams-Jones 1997).

If Fischer–Tropsch type synthesis did occur, then we should expect to see a range of light hydrocarbons with C_{n+1} carbon numbers in an ordered proportion. Although highly sensitive gas chromatography able to detect very low volumes of other $C_nH_{(2n+2)}$ hydrocarbons aside from ethane did not form part of this study, CH_4 and other light hydrocarbons have been detected in other orogenic gold deposits. The Sigma, Norbeau and Tadd deposits in Canada contain 14.38, 1.10 and 14.05 mol% CO_2, 16.23, 5.59 and 11.96 mol% CH_4, and 1.98, 0.32 and 2.31 mol% $C_nH_{(2n+2)}$, respectively (Graney & Keslar 1995). Similarly, up to 13.4% CO_2, 4950 ppm CH_4, trace C_2H_6, C_3H_8 and other light hydrocarbons were found in at least four different orogenic, lode-gold deposits hosted by mafic to ultramafic rocks in the Barberton greenstone belt, South Africa (Bray *et al.* 1991; De Ronde *et al.* 1992).

The reactions and reduced environment result in CH_4 being concentrated at the edges of many syn-gold quartz veins at Junction because fluid access to the ilmenite- and/or titanomagnetite-bearing Junction Dolerite was greatest in this area. Scanning electron microprobe data and petrographic investigations reveal that minor amounts of ilmenite and titanomagnetite are still present in the biotite–calcite zone (Figure 6). Therefore, the mineralised portion of the Junction shear zone was not only reduced to levels that promote CH_4 and ethane generation, but a Group VIII metal catalyst in the form of ilmenite or titanomagnetite was still present during the late stages of mineralisation when it is proposed that CH_4 generation took place. The reactions also explain the absence of CH_4 at the edges of some syn-gold quartz veins that occur within the biotite–calcite zone. It is possible that these veins precipitated earlier in the formation of the Junction shear zone when the oxidation state was higher and, thus, less conducive to CH_4 generation.

The hypothesis that CH_4 and ethane formed by the reduction of CO_2 in the Junction lode gold deposit illustrates and explains: (i) how the zonation of the CO_2:CH_4 ratios across the syn-gold quartz veins formed; (ii) the presence of ethane in the vein calcite from the biotite–calcite zone; and (iii) the relatively low levels of CH_4 in the vein calcite collected from the chlorite zone or the albite zone in which pyrrhotite is less abundant and the oxidation state was higher and, thus, less conducive to CH_4 generation.

Although Fischer–Tropsch type synthesis may seem unlikely, previous investigators have used it to explain the presence of oil in serpentinites (Friedel & Sharkey 1963) in which the H_2 is produced during serpentinisation, as is the catalyst (magnetite), and the carbon is juvenile (Szatmari 1989). Fischer–Tropsch type synthesis has also been invoked to explain the presence of hydrocarbons in meteorites (Studier *et al.* 1972). Therefore, although the CH_4-bearing fluid inclusions could have originated from fluid unmixing of a coexisting CO_2–CH_4-bearing fluid, or the post-entrapment alteration of the fluid inclusions, or the late introduction of a CH_4-rich fluid, we favour a process whereby CO_2 was reduced to CH_4 and traces of ethane as one that adequately explains and fits all of the available data.

CONCLUSIONS

Geological, thermometric and Raman data have identified three different vein systems that are associated with three distinct periods of geological time, which host four distinct fluid types that are now represented by a variety of fluid inclusions. These are:

(1) The Mo-type quartz veins that precipitated from a hot, highly saline, fluid that mixed with a cooler, less-saline fluid. Ultimately, this resulted in Mo-type fluid inclusions having mixed salinities and variable homogenisation temperatures. This event occurred before the development of the Junction shear zone.

(2) The syn-gold quartz veins are associated with an extensive biotite–calcite–quartz–albite–pyrrhotite–chlorite alteration assemblage. They precipitated from a hot, moderately saline, H_2O–CO_2 ($\pm$ CH_4) gold-bearing fluid that was introduced during the development of the Junction shear zone. Two independent geothermometers indicate that the ambient temperature for deposit formation was approximately 400°C. Pressure fluctuations varied from 70 MPa to 440 MPa. Fluid unmixing associated with pressure fluctuation along the Junction shear zone produced a spectrum of fluid inclusions that range from low salinity, CO_2-rich compositions to higher salinity, aqueous-rich compositions. Fluid unmixing is supported by the presence of free gold and the fact that some fluid inclusions in the same sample homogenise into either the vapour phase or the liquid phase over the same temperature range.

(3) Post-gold quartz veins precipitated from a hot, CO_2>H_2O–CH_4-bearing fluid that penetrated normal fault sets, which displaced the foliation in the Junction shear zone. This displacement indicates that they formed after the gold-mineralising event ended. Total homogenisation temperatures between 271.1°C and 313.2°C are in approximate agreement with formation temperatures that range from 289°C to 359°C, which were calculated by oxygen isotope geothermometry. This indicates that the homogenisation temperatures are close to the entrapment temperature and that a maximum pressure correction in the order of 50°C may be required for this vein type.

(4) Late secondary fluid inclusions reveal that a moderately hot, highly saline, H_2O–$CaCl_2$–$NaCl$-bearing fluid that precipitated halite and trapped carbonate daughter minerals percolated through and was trapped along fluid inclusion trails that formed late in the deposits history.

Of significant interest to this deposit type is the fact that many syn-gold quartz veins at Junction are zoned with respect to the CO_2:CH_4 ratios in fluid inclusions. CH_4-bearing fluid inclusions occur in quartz grains that are associated with the alteration assemblage that occurs almost exclusively at the vein margin, whereas fluid inclusions hosted in quartz grains found toward the centre of the same vein are pure CO_2 or contain trace amounts of CH_4. Follow-up work reveals that elevated CH_4 volumes are restricted within the Junction shear zone to the area of biotite–calcite–pyrrhotite mineralisation, suggesting that a relationship exists between the biotite–calcite zone and CH_4.

Although a CH_4-bearing fluid could have originated from a crustal source, or be generated during the ascension of a hydrothermal fluid through graphitic units, this paper

has demonstrated that the gold-bearing fluid probably contained only trace CH_4. Fluid unmixing, post-entrapment alteration of fluid inclusions and/or the late introduction of a CH_4-rich fluid cannot adequately account for the zonation of $CO_2:CH_4$ ratios across the quartz–calcite veins or explain the relative absence of CH_4 in the calcite phase of the quartz–calcite veins that extend into the chlorite zone and the albite zone. Alternatively, the reduction of CO_2 to CH_4 during a process similar to Fischer–Tropsch type synthesis does explain why CH_4 is found at the edges of the quartz veins and why there are relatively low levels of CH_4 in the vein calcite collected from the chlorite zone or the albite zone. Finally, given that microthermometric and Raman spectroscopic data indicate that fluid inclusions in the Junction deposit are thermodynamically and compositionally similar to fluid inclusions reported from other orogenic lode-gold deposits, it is possible that CO_2 and CH_4 zoning across mineralised quartz veins is not unique to the Junction deposit.

ACKNOWLEDGEMENTS

REFERENCES

ANDERSON R. B. 1984. *The Fischer–Tropsch Synthesis*: Academic Press, New York.

BODNAR R. J. 1993. Revised equation and table for determining the freezing point depression of H_2O–NaCl solutions. *Geochimica et Cosmochimica Acta* **57**, 683–684.

BOULLIER A-M. & ROBERT F. 1992. Paleoseismic events recorded in the Archaean gold–quartz vein networks, Val d'Or Abitibi, Quebec. *Journal of Structural Geology* **14**, 161–179.

BOULTER C. A., FOTIOS M. G. & PHILLIPS G. N. 1987. The Golden Mile, Kalgoorlie: a giant gold deposit localized in ductile shear zones by structurally induced infiltration of an auriferous metamorphic fluid. *Economic Geology* **82**, 1661–1678.

BOWERS T. S. & HELGESON H. C. 1983a. Calculations of the thermodynamic and geochemical consequences of non-ideal mixing in the system H_2O–CO_2–NaCl on phase relations in geological systems: equations of state for H_2O–CO_2–NaCl fluids at high pressure and temperature. *Geochimica et Cosmochimica Acta* **47**, 1247–1275.

BOWERS T. S. & HELGESON H. C. 1983b. Calculations of the thermodynamic and geochemical consequences of non-ideal mixing in the system H_2O–CO_2–NaCl on phase relations in geological systems: metamorphic equilibria at high pressures and temperatures. *American Mineralogist* **68**, 1059–1075.

BRAY C. J. & SPOONER E. T. C. 1992. Fluid inclusion volatile gases by gas chromatography with photoionization/microthermal conductivity detectors: applications to magmatic MoS_2 and other H_2O–CO_2 and H_2O–CH_4 fluids. *Geochimica et Cosmochimica Acta* **56**, 261–272.

BRAY C. J., SPOONER E. T. C. & THOMAS A. V. 1991. Fluid inclusion volatile analysis by heated crushing, on-line gas chromatography: application to Archaean fluids. *Journal of Geochemical Exploration* **42**, 167–192.

BROWN P. E. & HAGEMANN S. G. 1995. MacFlinCor and its application to fluids in Archean lode-gold deposits. *Geochimica et Cosmochimica Acta* **59**, 3943–3952.

CAREY M. L. 1994. Petrography and geochemistry of selected sills from the Kambalda–Kalgoorlie region, WA. BSc (Hons) thesis, Australian National University, Canberra (unpubl.).

CLAOUÉ-LONG J. C., COMPSTON W. & COWDEN A. 1988. The age of the Kambalda greenstones resolved by ion-microprobe: implications for Archaean dating methods. *Earth and Planetary Science Letters* **89**, 239–259.

CLARK M. E., CARMICHAEL N. J., HODGSON C. J. & FU M. 1989. Wall-rock alteration, Victory gold mine, Kambalda, Western Australia. *In*: Keays R. R., Ramsay W. R. H. & Groves D. I. eds. *The Geology of Gold Deposits: the Perspective in 1988*, pp. 445–459. Economic Geology Monograph **6**.

CLAYTON R. N., O'NEIL J. R. & MAYEDA T. K. 1972. Oxygen isotope exchange between quartz and water. *Journal of Geophysical Research* **67**, 3057–3067.

COLLINS P. L. F. 1979. Gas hydrates in CO_2-bearing fluid inclusions and the use of freezing data for estimation of salinity. *Economic Geology* **74**, 1435–1444.

COLVINE A. C., FYON J. A., HEATHER K. B., MARMONT S., SMITH P. M. & TROOP D. G. 1988. Archean lode-gold deposits in Ontario. *Geological Survey of Ontario Miscellaneous Paper* **139**.

DAVIS D. W., LOWENSTEIN T. K. & SPENCER R. J. 1990. Melting behaviour of fluid inclusions in laboratory-grown halite crystals in the systems NaCl–H_2O, NaCl–KCl–H_2O, NaCl–$MgCl_2$–H_2O and NaCl–$CaCl_2$–H_2O. *Geochimica et Cosmochimica Acta* **54**, 591–601.

DE RONDE C. E. J., SPOONER E. T. C., DE WIT M. J. & BRAY C. J. 1992. Shear zone-related, Au quartz vein deposits in the Barberton Greenstone Belt, South Africa: field and petrographic characteristics, fluid properties, and light stable isotope geochemistry. *Economic Geology* **87**, 366–402.

DUAN Z., MOLLER N. & WEARE J. H. 1992a. An equation of state for the CH_4–CO_2–H_2O system: I. Pure Systems from 0 to 1000°C and 0–8000 bar. *Geochimica et Cosmochimica Acta* **56**, 2605–2617.

DUAN Z., MOLLER N. & WEARE J. H. 1992b. An equation of state for the CH_4–CO_2–H_2O system: II. Mixtures from 50 to 1000°C and 0–1000 bar. *Geochimica et Cosmochimica Acta* **56**, 2619–2631.

ELLERY S. & WATTS D. 1996. WMC St Ives Gold. Junction North surface geology: 1:7500 scale map. WMC Resources (unpubl.).

FERGUSON J. 1987. A possible role for light hydrocarbons in Pb/Zn mineral exploration. *Mineralogical Magazine* **51**, 527–533.

FRIEDEL R. A. & SHARKEY A. G. 1963. Alkanes in natural and synthetic petroleum: comparison of calculated and actual compositions. *Science* **139**, 1203–1205.

GEBRE-MARIAM M., GROVES D. I. & MCNAUGHTON N. J. 1997. Aqueous and CO_2- and CH_4-rich inclusions at the Archean Golden Kilometre gold deposit: multiple fluid sources and depositional mechanisms. *Chronique de la Recherche Miniere* **529**, 59–73.

GOLDING S. D., CLARK M. E., KEELE R. A., WILSON A. F. & KEAYS R. R. 1990. Geochemistry of Archaean epigenetic gold deposits in the Eastern Goldfields Province, Western Australia. *In*: Herbert H. K. & Ho S. E. eds. *Stable Isotopes and Fluid Processes in Mineralisation*, p. 23. Geology Department and University Extension, University of Western Australia, Nedlands.

GRANEY J. R. & KESLAR S. E. 1995. Gas composition of fluid in ore deposits: is there a relation to magmas? *In*: Thompson J. F. H. ed. *Magmas, Fluids and Ore Deposits*, pp. 221–245. Mineralogical Association of Canada Short Course Series **23**.

HAGEMANN S. G., BRAY C., BROWN P. E. & SPOONER E. T. C. 1996. Combined gas and ion chromatography of fluid inclusions and sulfides from the Archean epizonal Wiluna lode gold deposits, Western Australia. *In*: Brown P. E. & Hagemann S. G. eds. *Pan-American Conference on Research on Fluid Inclusions 6: Programs and Abstracts*, pp. 56–58. Department of Geology and Geophysics, University of Wisconsin, Madison.

HAGEMANN S. G. & CASSIDY K. F. 2000. Archean orogenic lode gold deposits. *Reviews in Economic Geology* **13**, 9–68.

HALL D. L. & BODNAR R. J. 1990. Methane in fluid inclusions from granulites: a product of hydrogen diffusion? *Geochimica et Cosmochimica Acta* **54**, 641–651.

HO S. E. 1987. Fluid inclusions: their potential as an exploration tool for Archaean gold deposits. *In*: Ho S. E. & Groves D. I. eds. *Recent Advances in Understanding Precambrian Gold Deposits*, pp. 239–263. Geology Department and University Extension, University of Western Australia Publication **11**.

HO S. E., BENNETT J. M., CASSIDY K. F., HRONSKY J. M. A., MIKUCKI E. J. & SANG J. H. 1990b. Nature of ore fluid, and transportational and depositional conditions: fluid inclusion studies. *In*: Ho S. E., Groves D. I. & Bennett J. M. eds. *Gold Deposits of the Archaean Yilgarn Block, Western Australia: Nature Genesis and Exploration Guides*, pp. 198–211. Geology Department (Key Centre) and University Extension, University of Western Australia Publication **23**.

HO S. E., GROVES D. I., MCNAUGHTON N. J. & MIKUCKI E. J. 1992. The source of ore fluids and solutes in Archean lode-gold deposits of Western Australia. *Journal of Volcanology and Geothermal Research* **50**, 173–196.

HO S. E., GROVES D. I. & PHILLIPS G. N. 1990a. Fluid inclusions in quartz veins associated with Archaean gold mineralisation: clues to ore fluids and ore depositional conditions and significance to exploration. *In*: Herbert H. K. & Ho S. E. eds. *Stable Isotopes and Fluid Processes in Mineralisation*, pp. 35–50. Geology Department and University Extension, University of Western Australia Publication **20**.

JACOBS G. K. & KERRICK D. M. 1981. Methane: an equation of state with application to the ternary system $H_2O–CO_2–CH_4$. *Geochimica et Cosmochimica Acta* **45**, 607–614.

LIU L. G. & MERNAGH T. P. 1990. Phase transitions and Raman spectra of calcite at high pressures and room temperature. *American Mineralogist* **75**, 801–806.

MAVROGENES J. A. & BODNAR R. J. 1994. Experimental evidence and geological implications of hydrogen movement into and out of fluid inclusions in quartz. *Geochimica et Cosmochimica Acta* **59**, 3987–3995.

MERNAGH T. P. 1996. Gold mineralisation at Mt Charlotte: evidence for fluid oxidation from fluid inclusions. *Geological Society of Australia Abstracts* **41**, 292.

MIKUCKI E. J. 1998. Hydrothermal transport and depositional processes in Archean lode-gold systems: a review. *Ore Geology Reviews* **13**, 307–321.

MIKUCKI E. J. & RIDLEY J. R. 1993. The hydrothermal fluid of Archaean lode-gold deposits: constraints on its composition inferred from ore and wallrock alteration assemblages over a spectrum of metamorphic grades. *Mineralium Deposita* **28**, 469–481.

MURPHY T. E. 1995. An investigation into the petrology and geochemistry of the felsic to intermediate intrusions within the Junction gold mine, Kambalda, Western Australia; and their relationship to gold mineralisation. BSc (Hons) thesis, University of Technology, Sydney (unpubl.).

NADEN J. & SHEPHERD T. J. 1989. Role of methane and carbon dioxide in gold deposition. *Nature* **342**, 793–795.

NELSON D. R. 1995. Compilation of SHRIMP U–Pb zircon geochronology data, 1994. *Geological Survey of Western Australia Records* **1995/3**.

O'NEIL J. R., CLAYTON R. N. & MAYEDA T. K. 1969. Oxygen isotope fractionations in divalent metal carbonates. *Journal of Chemical Physics* **51**, 5547–5558.

PHILLIPS G. N. 1986. Geology and alteration in the Golden Mile, Kalgoorlie. *Economic Geology* **81**, 779–808.

PHILLIPS G. N. & GROVES D. I. 1983. The nature of Archaean gold-bearing fluids as deduced from gold deposits of Western Australia. *Journal of the Geological Society of Australia* **30**, 25–39.

POLITO P. A. 1999. Exploration implications predicted by the distribution of carbon–oxygen–hydrogen gases above and within the Junction gold deposit, Kambalda, Western Australia. PhD thesis, University of Adelaide, Adelaide (unpubl.).

ROBERT F., BOULLIER A. & FIRDAOUS K. 1995. Gold–quartz veins in metamorphic terranes and their bearing on the role of fluids in faulting. *Journal of Geophysical Research* **100**, 12 861–12 879.

ROBERT F. & KELLY W. C. 1987. Ore-forming fluids in Archean gold-bearing quartz veins at the Sigma Mine, Abitibi greenstone belt, Quebec, Canada. *Economic Geology* **82**, 1464–1482.

ROBERT F., POULSEN K. H. & DUBE B. 1994. *Structural Analysis of Lode-gold Deposits in Deformed Terranes*. Geological Survey of Canada, Ottawa.

ROBERTS D. E. & ELIAS M. 1990. Gold deposits of the Kambalda – St Ives region. *In*: Hughes F. E. ed. *Geology of the Mineral Deposits of Australia and Papua New Guinea*, pp. 479–491. Australasian Institute of Mining and Metallurgy, Melbourne.

SALVI S. & WILLIAMS-JONES A. E. 1997. Fischer–Tropsch synthesis of hydrocarbons during sub-solidus alteration of the Strange Lake peralkaline granite, Quebec/Labrador, Canada. *Geochimica et Cosmochimica Acta* **61**, 83–99.

SHEPHERD T. J., RANKIN A. H. & ALDERTON D. H. M. 1985. *A Practical Guide to Fluid Inclusion Studies*. Blackie and Sons, New York.

SIBSON R. H., ROBERT F. & POULSEN K. H. 1988. High angle reverse faults, fluid-pressure cycling and mesothermal gold–quartz deposits. *Geology* **16**, 551–555.

SPRY P. G., PAREDES M. M., FOSTER F., TRUCKLE J. S. & CHADWICK T. H. 1996. Evidence for a genetic link between gold–silver telluride and porphyry molybdenum mineralisation at the Golden Sunlight Deposit, Whitehall, Montana: fluid inclusion and stable isotope studies. *Economic Geology* **91**, 507–526.

STUDIER M. H., HAYATSU R. & ANDERS E. 1972. Origin of organic matter in early solar system. V. Further studies of meteoric hydrocarbons and a discussion of their origin. *Geochimica et Cosmochimica Acta* **36**, 189–215.

SZATMARI P. 1989. Petroleum formation by Fischer–Tropsch synthesis in plate tectonics. *American Association of Petroleum Geologists Bulletin* **73**, 989–998.

TAKENOUCHI S. & KENNEDY G. C. 1965. The solubility of carbon dioxide in NaCl solution at high temperatures and pressures. *American Journal of Science* **263**, 445–454.

VAN DEN KERKHOF A. M., TOURET J. L. R., MAIJER C. & JANSEN J. B. H. 1991. Retrograde methane-dominated fluid inclusions from high temperature granulites of Rogaland, southwestern Norway. *Geochimica et Cosmochimica Acta* **55**, 2533–2544.

VAUGHAN D. J. & CRAIG J. R. 1997. Sulphide ore mineral stabilities, morphologies, and intergrowth textures. *In*: Barnes H. L. ed. *Geochemistry of Hydrothermal Ore Deposits*, pp. 367–434. John Wiley and Sons, New York.

WATCHORN R. B. 1998. Kambalda – St Ives gold deposits. *In*: Berkman D. A. & Mackenzie D. H. eds. *Geology of Australian and Papua New Guinean Mineral Deposits*, pp. 243–254. Australasian Institute of Mining and Metallurgy, Melbourne.

WITT W. K. 1992. Gold deposits of the Kalgoorlie–Kambalda—St Ives area, Western Australia. *Geological Survey of Western Australia Record* **1992/15**.

WITT W. K., HICKMAN A. H., TOWNSEND D. & PRESTON W. A. 1998. Mineral potential of the Archaean Pilbara and Yilgarn Cratons, Western Australia. *AGSO Journal of Australian Geology & Geophysics* **17**, 201–221.

WITT W. K., KNIGHT J. T. & MIKUCKI E. J. 1997. A synmetamorphic lateral fluid flow model for gold mineralisation in the Archean Southern Kalgoorlie and Norseman Terranes, Western Australia. *Economic Geology* **92**, 407–437.